TÉCNICO LISBOA

Techno-economic assessment of 20MW floating wind turbines

Humberto João Sousa Leite da Silva

Thesis to obtain the Master of Science Degree in

Aerospace Engineering

Supervisors: Professor Luís Rego da Cunha de Eça
Doctor Marco Aurélio de Araújo Alves

Examination Committee

Chairperson: Professor Filipe Szolnoky Ramos Pinto Cunha
Supervisor: Doctor Marco Aurélio de Araújo Alves
Member of the Committee: Eng.º Miguel Jorge Marques

November 29, 2019

Dedicated to my godmother

Acknowledgments

I would like to express my gratitude to Dr. Marco Alves, from WavEC - Offshore Renewables, for suggesting the topic of my mater's thesis and making it possible for me to work in the interesting field that is the floating offshore wind industry.

I express my gratitude as well to my thesis supervisor, Professor Luís Eça, from IST. His knowledge of the field, constant support and remarks throughout the writing of this thesis were fundamental for me to complete it.

Also, to all the WavEC personnel for welcoming me in their team. Especially to Miguel Vicente for the help with the WAMIT simulations and his insight whenever asked.

I deeply thank my parents and sisters for the unconditional support and for making it possible for me to focus on my degree during this years.

To all my friends, that always have time for a Saturday night reunion. A special shout out to my DotA partners, because the laughs and distractions in these games can never be disregarded during such a long project.

Lastly, to Daniela that was always there for me, cheering me up in the lows, never letting me give up, and making the good moments even better.

This work is financially supported by national funds through the FCT/MCTES (PIDDAC), under the project PTDC/ECI-EST/29558/2017.

FCT
Fundação para a Ciência e a Tecnologia
MINISTÉRIO DA CIÊNCIA, TECNOLOGIA E ENSINO SUPERIOR

Resumo

A crescente procura de energia, especialmente de fontes renováveis, exige soluções mais eficientes. Turbinas eólicas com potência nominal mais elevada, localizadas mais longe da costa, onde as condições são mais favoráveis para a produção de energia, irão marcar o futuro do setor *offshore*. No entanto, águas mais profundas tornam essencial a utilização de plataformas flutuantes para haver viabilidade tecno-económica.

Esta tese apresenta a ampliação de uma turbina eólica *offshore* flutuante de 8 MW para 20MW. Este estudo está dividido em três partes: estimativa do erro numérico das simulações realizadas para a turbina de 8 MW, de modo a selecionar as configurações numéricas do OpenFAST; dimensionamento da configuração de 20MW e testá-la sob várias condições operacionais; estimativa do custo nivelado de energia para a turbina de 20 MW.

A precisão numérica do modelo de 8MW é afetada por um compromisso entre tempo e recursos computacionais, mas os resultados mostram que é possível ter confiança na solução com base nas configurações escolhidas. Após o *upscale* para uma configuração de 20 MW, recorrendo a regras clássicas de semelhança, foram testadas a estabilidade hidrostática e o comportamento dinâmico do sistema sob várias condições operacionais, mostrando grande estabilidade. Na realidade, pode haver margem para usar uma plataforma mais pequena com uma abordagem menos conservadora.

O modelo tecno-económico mostrou que a turbina de 20MW ainda não consegue competir com outras fontes de energia, mas permite concluir que existem formas de reduzir o custo nivelado de energia no futuro.

Palavras-chave: turbina eólica *offshore* flutuante, simulação numérica, precisão numérica, ampliação, custo nivelado de energia.

Abstract

The increasing energy demand, especially from renewable sources, calls for more efficient solutions. Wind turbines with higher rated power, deployed further offshore where the conditions are more favourable for energy production, will mark the future standards in the offshore industry. However, deeper waters make the use of floating platforms essential for their techno-economic feasibility.

This thesis presents the upscaling of an 8MW floating offshore wind turbine to 20MW. The study is divided in three phases: estimation of the numerical accuracy of the simulations performed for the 8MW turbine to select the numerical settings for OpenFAST; scaling to a 20MW configuration and test it under several load cases; make an estimation of the levelized cost of energy for the 20MW turbine.

The numerical accuracy of the 8MW model is affected by a compromise between time and computation capacity, but the results show that one can have confidence on the solution based on the settings chosen. After scaling to a 20MW configuration using classic similarity rules, the hydrostatic stability and dynamic behaviour under several load cases were tested, showing great stability. In fact, there might be margin to use a smaller platform with a less conservative approach.

The techno-economic model showed that the system is still unable to compete with other sources of energy, but allows to conclude that there are ways of reducing the levelized cost of energy in the future.

Keywords: floating offshore wind turbine, numerical simulation, numerical accuracy, upscaling, levelized cost of energy.

Contents

List of Tables

List of Figures

Nomenclature

Greek symbols

Δ	Water displacement
δ	Kronecker-Delta function
γ	Peak shape parameter
λ	Dimentionless catenary parameter
μ	Mass per unit length of mooring line
Ω	Angular rotation velocity of the rotor
ω	Wave frequency
ϕ	Sum of atack and pitch angles of the blade
ρ	Density
σ	Scaling factor
ζ	Wave elevation

Roman symbols

$\ddot{q}$	Acceleration
$\dot{q}$	Velocity
A	Added-mass matrix
A	Water-plane area
a	Axial induction factor
a'	Rotational induction factor
C	Linearized restoring matrix of all moorings
g	Gravitational acceleration constant
I	Moment of inertia of the water-plane area

K	Wave-radiation retardation Kernel
L	Unstretched mooring length
M	Inertia mass matrix
q	Displacement in a degree of freedom
r	Radial position on the blade
sf	Geometric scaling factor
t	Time
V	Volume of displaced water
w	Apparent weight in fluid per unit length

Acronyms

AEP Annual Energy Production

BEM Blade element momentum

CAD Computer-Aided Design

CAE Computer-Aided Engineering

CAPEX Capital expenditures

CM Centre of mass

COB Centre of buoyancy

DTU Danmarks Tekniske Universitet

FAST Fatigue, Aerodynamics, Structures and Turbulence

FOWT Floating offshore wind turbine

JONSWAP Joint North Sea Wave Project

LCOE Levelized cost of energy

MIT Massachusetts Institute of Technology

NASA National Aeronautics and Space Administration

NREL National Renewable Energy Laboratory

NWTC National Wind Technology Center

O&M Operation and maintenance

OC3 Offshore Code Comparison Collaboration

OC4 Offshore Code Comparison Collaboration Continuation

OPEX Operational expenditures

RMS Root mean square

TLP Tension-leg platform

TRL Technology Readiness Level

WGN White Gaussian noise

Chapter 1

Introduction

Wind energy has been largely used by humans to sail ships, grind grain and pump water for thousands of years, but it was only in the late nineteenth century that it was used to produce electricity in Scotland. The oil crisis in the 1970s led to a bigger investment in wind energy sector and, in 1975, NASA started a program to develop utility-scaled wind turbines and this research was the pioneer of some of the multi-megawatt turbines in use today. It started a fast evolution in the design of wind turbines, achieving greater rated power, size and better efficiency, which leads to a reduction of the LCOE.

The first offshore wind turbine was built in Denmark in 1980, bringing new challenges to the industry [1]. As the turbines get bigger, larger areas with steadier winds are required, so the solution is to go offshore, where water depths can exceed several hundred meters.

At depths beyond 60 to 90 meters, bottom-fixed structures stop being economically viable, which creates the necessity to use floating solutions. However, floating platforms further from the coast are more expensive, thereby the electricity generation has to be reliable to ensure economic feasibility.

The objective of this thesis is to scale a 8MW wind turbine to a 20MW rating. The smaller turbine is subjected to a series of tests to estimate the accuracy of the solution. Also, a statistical convergence study is conducted. This ensures that a base is laid on how further simulations should be conducted to analyse the behaviour of the 20MW floating wind turbine. The scaling approach is presented and a techno-economic study is done with the objective of getting a rough estimation of the LCOE.

There is an obvious analogy between the blades of a wind turbine and the wings of an plane, which means that the advances in the wind energy field can always be translated to the aerospace sector, and vice-versa.

1.1 Motivation and Background

As of now, the use of fossil fuels for energy supply is becoming unbearable. Climate change and the severe environmental consequences these sources bring, allied with the increase in energy demand at an unprecedented rate, are making the world shift towards renewable and more sustainable energy sources.

As a matter of fact, in 2018 the total wind capacity installed in Europe already covers 18.8% of the electricity demand of the European Union's 27 countries. It makes a total of 189GW of cumulative wind power capacity installed, from which around 10% comes from offshore installations. [2]

Although, onshore installations are reaching its limit, especially in areas with high population density. Actually, 2018 was the lowest year for new onshore installations in a decade. This facts motivate the countries and the investors to deploy wind turbines offshore. A number of the most relevant advantages of taking wind farms further away from the coastline are listed bellow:

- Stronger and more steady wind with less turbulence intensity and smaller shear,
- No limitation to the size of an offshore wind turbine if it can be manufactured near the coastline, i.e. no dealing with road or rail logistical constraints,
- Vast availability of sea surface and less problems with space occupation,
- Less problems dealing with noise pollution and visual impact.

On the other hand, offshore wind turbines imply higher capital investment, more challenging structural design, less accessibility, higher costs related to maintenance issues and electric power transmission to shore [3]. This is why wind turbines with high rated power, from 5 to 10MW now and up to 20MW in the near future, are needed. Only this magnitude of power ratings can make offshore wind feasible, especially for floating wind turbines.

1.2 Offshore wind structures

Offshore wind turbine support structures can be classified in three categories according to the water depth of the site where they are installed:

- Shallow water, if the water depth is less than 30 meters,
- Transitional water, if the water depth is between from 30 to 60 meters,
- Deep water, if water depth is bigger than 60 meters.

Figure 1.1 shows the support platforms according to the water depth of the deployment site.

As it was already stated, the conditions further offshore are more favourable than near the coastline. So, the tendency is to take the wind farms to deeper waters, where bigger turbines can be proved more cost-effective. This means floating platforms are the long term solution for the offshore wind farms in deep waters, instead of bottom-fixed. To prove this point, there is the relations water depth and cost of offshore wind turbine substructure in figure 1.2.

1.2.1 Floating platforms

There are currently four types of platform designs: barge, semi-submersible, spar and tension-leg platform (TLP), all represented in figure 1.3. While the technology readiness level of the semi-submersible

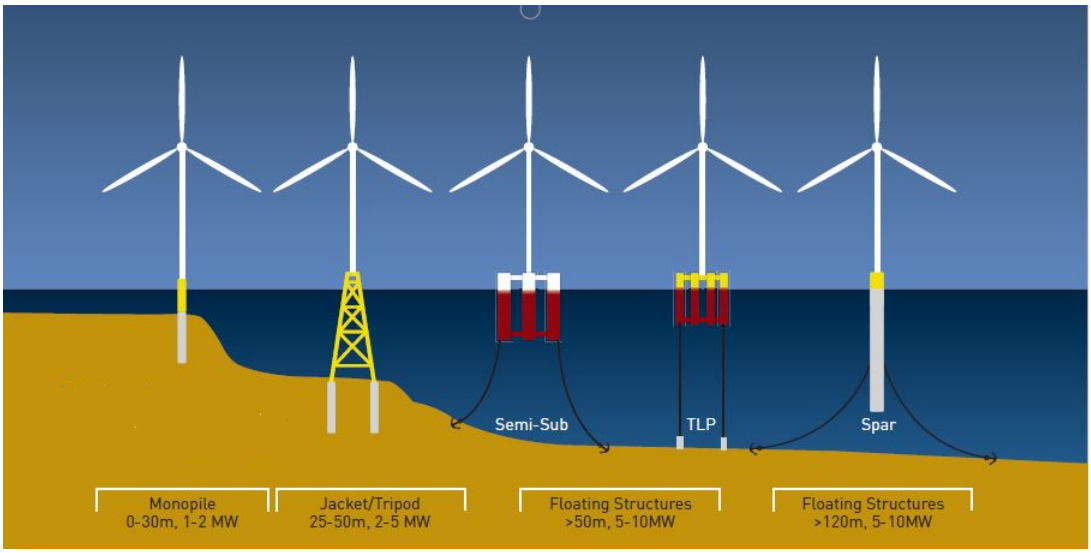

Figure 1.1: Wind turbine evolution from onshore to offshore sites [4]

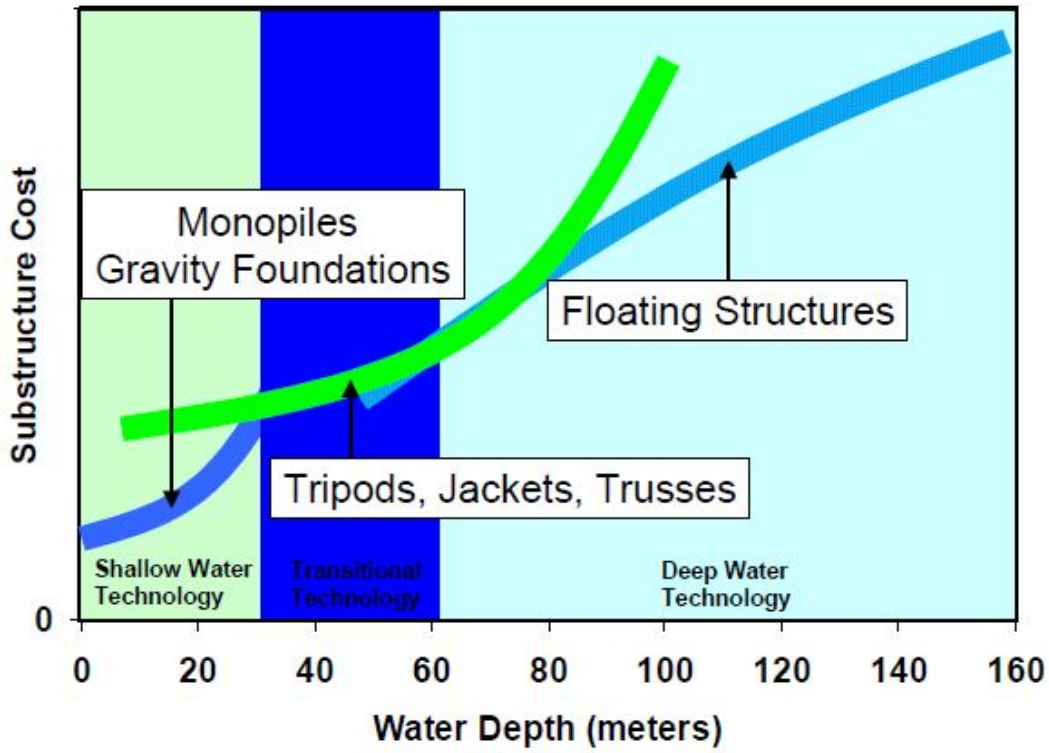

Figure 1.2: Variation of the cost of offshore wind substructures with water depth [5]

and spar has entered a stage where it is ready to be deployed, barge and TLP concepts are not ready for now [6]. In fact, the spar and semi-submersible concepts are already proven concepts with real scale prototypes tested and pre-commercial projects ongoing, like the WindFloat Atlantic project.

An explanation of how the several types of floating structures achieve stability and some of their advantages and disadvantages is now presented.

- **Barge:** stability obtained due to a large water plane area moment, which is a direct result of its large diameter and shallow draft. This concept has the setback of having large pitch and roll

motions when excited by waves. This restricts the deployment sites to harbours and lagoons.

- **Semi-submersible:** achieves stability between a combination of ballast and water plane stiffness. This kind of design has a shallow draft, when compared with the spar, which allows it to be deployed in a wider range of depths and has catenary mooring lines for station keeping.

- **Spar:** deep draft slender cylinder that obtains stability entirely because of a very low centre of gravity, which is due to the existence of ballast. The deep draft does not allow the deployment in shallow waters and can constraint the catenary mooring lines used to attach it to the seabed. It can either be made from steel or concrete.

- **Tension-leg platform:** maintains stability because the buoyant platform is connected to the sea bed trough tensioned mooring lines. Since the buoyancy is bigger than the displacement, it needs the tensioned lines to achieve equilibrium. This allows a smaller structure, but increases the complexity of the mooring system and the anchors.

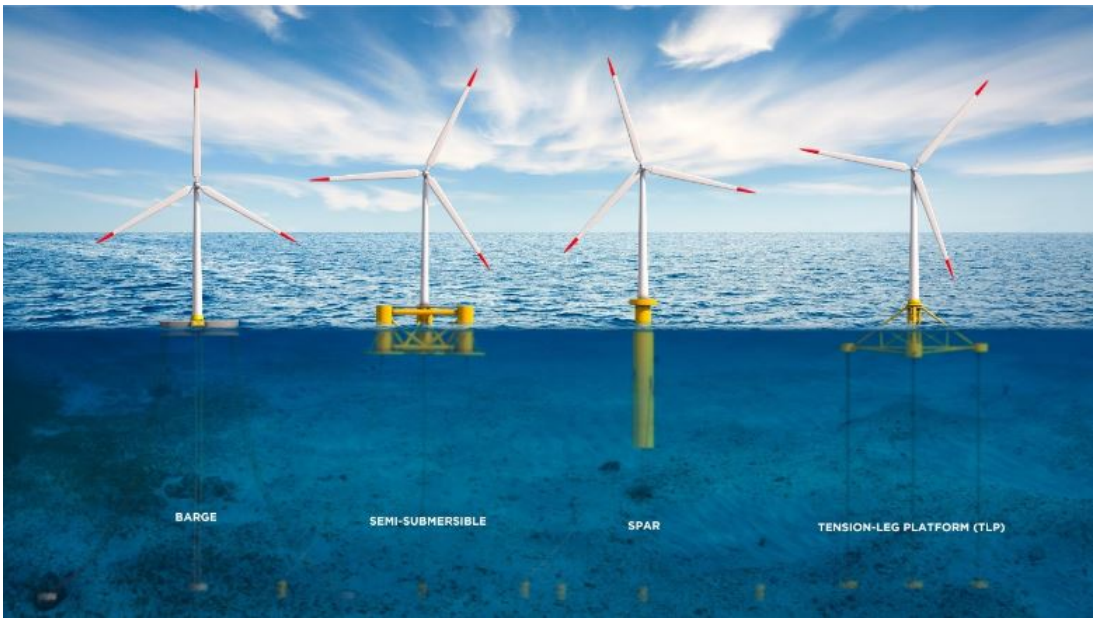

Figure 1.3: Main floating platform concepts [6]

It is important to add the note that there is an hybrid concept between fixed bottom and floating structures that is mentioned, the gravity based foundations. This kind of structures can be carried floating to the site of deployment and only there they are submerged. Even though this is a characteristic that makes them attractive in terms of the installation process, they still can only be used in shallow waters, which means that in deep waters it is still the floating platforms that are economically feasible.

Figure 1.4: Windfloat semi-submersible design with wind turbine.

1.3 Ongoing Projects

Windfloat Atlantic

WindFloat is a floating foundation for offshore wind turbines. It is a semi-submersible consisting of three cylindrical columns arranged in a triangular shape with the turbine placed in one of the columns. Each column has a hexagonal heave plate on the submerged end to provide dynamic stability. Principle Power holds the patent for this technology which has in MiniFloat its predecessor. [4]

One advantage of this design is the great stability performance that allows the use of existing wind turbine technology with few modifications. A contributing part for this comes from the active hull trim system, that allows ballast water to move from column to column. In theory, it allows a mean pitch of 0°, while it should be around 4° without it, optimizing energy production. [7]

This project is the follow-up of the first large-scale test of a semi-submersible platform, the DemoFloat. The Windfloat platform equipped with a 2MW wind turbine was deployed 5km off the cost of Portugal and operated between 2011 and 2016, when it was successfully decommissioned and dissembled at quayside. This period of operation in harsh Atlantic ocean conditions, with wave significant heights reaching up to 17 meters, provided data to validate the concept. WindFloat Atlantic is next step, the pre-commercial phase. Three 8.3 MW wind turbines located 20km off the coast of Viana do Castelo in Portugal, at a water depth of 100 meters, began to be deployed in October. It is schedule to be fully commissioned by the end of 2019. [8]

Figure 1.5 illustrates the several stages of the evolution of the WindFloat technology and, as stated above, the pre-commercial phase in ongoing.

There are projects being planned for the next 5 to 10 years with this design in the US (Hawaii, 2 x 408 MW), Scotland (Kincardine, 48-50 MW) and South Korea (Ulsan, 500 MW). [9]

Phase 1 – 2 MW Prototype	Phase 2 – Pre-Commercial	Phase 3 – Comercial
• 2MW Prototype in Aguçadoura • ~5 km of the coast in 40-50m water depth • 12 months monitoring period • Validation criteria for acceptance	• Controlled roll-out with the deployment of 3 to 5 commercially optimized devices (5MW or greater) • Deployment off Portuguese west coast, grid connected	• Up to 150 MW deployment • Serial production and pre-fabrication of components • Grid connected with 5MW OWTG • Location TBD

Figure 1.5: Phases of Windfloat project evolution [7].

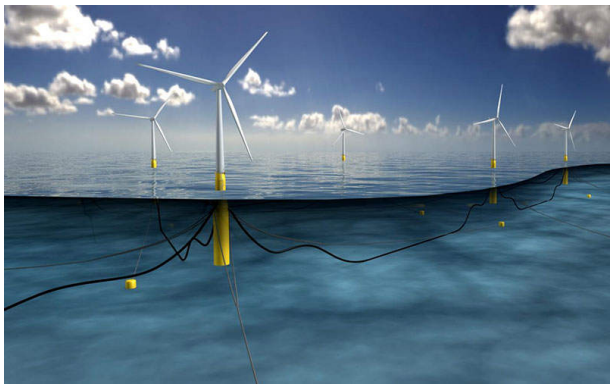

Figure 1.6: Hywind spar-buoy.

Hywind

The Hywind spar-buoy is one of the most proved concepts for floating offshore wind. A 2.3MW prototype was deployed in Norway in 2009 and was in operation until 2015. The concept consists in a classical deep draft spar buoy with three catenary mooring lines. [9]

A pre-commercial project has been put in operation by Statoil in 2017 off the coast of Scotland. It consists in five turbines with a 6MW rating, making it a 30MW project with capacity to supply up to 20 000 homes. It has an expected operational lifespan of 20 years. [10]

Floatgen

Figure 1.7: Floatgen floating wind turbine.

Floatgen uses Ideol's damping pool technology as the supporting platform for the turbine. It consists in a square concrete hull with a central opening to form a damping pool. Fundamentally, it uses the entrapped water to minimize floater motions, so it has a strong hydrodynamic performance. As a consequence, it can use regular commercial wind turbines with only a few modifications [9]. It can be classified as a barge type of floating platform because of its low draft.

Built around a European consortium of seven partners, a demonstration prototype of this technology was deployed off the coast of Le Croisic [11]. A 2MW wind turbine supported on Ideol's damping pool was fully commissioned in the middle of 2018 and has been providing results since then, being now fully validated and ready for commercial-scale deployment. [12]

1.4 Numerical Tools

Several numerical tools were used to simulate the dynamic response of the floating wind turbine. NREL's aero-hydro-servo-elastic code was the main tool used, while others were mainly used in the preprocessing of data to be used by some of the OpenFAST's modules.

OpenFAST

OpenFAST is the most recent version of FAST (Fatigue, Aerodynamics, Structures and Turbulence), a CAE tool developed by NREL's National Wind Technology Center (NWTC) to model, initially, onshore wind turbines. Then, its capabilities were extended to include the platform and mooring dynamics, enabling the simulation of floating offshore wind turbines. The software joins "aerodynamics models, hydrodynamics models for offshore structures, control and electrical system (servo) dynamics models, and structural (elastic) dynamics models to enable coupled non-linear aero-hydro-servo-elastic simulation in the time domain" [13]. OpenFAST has a modularized framework to include all these features [14]. The modules used in this work are AeroDyn, HydroDyn, ServoDyn, ElastoDyn, MoorDyn and InflowWind and their integration is described in figure 2.1. The OC3 and OC4 projects made a comparison between several codes and uses the data gathered in wave tanks tests to assess the accuracy of the turbine models simulated.

WAMIT

WAMIT (Wave Analysis at MIT) provided coefficients for the HydroDyn module. It uses potential flow theory to analyse wave interactions with offshore platforms and other structures or vessels. Using the geometry file of the floating platform generated by a Matlab script, WAMIT computes the added-mass, damping and stiffness matrices that will be used by HydroDyn.

TurbSim

TurbSim is a stochastic, turbulent wind generator for FAST code. It simulates numerically time series of three-component wind-speed vectors at points of a two-dimensional vertical rectangular grid that is user-

defined and fixed in space. The output from TurbSim is used by FAST through the module InflowWind, as seen in figure 1.8. [15]

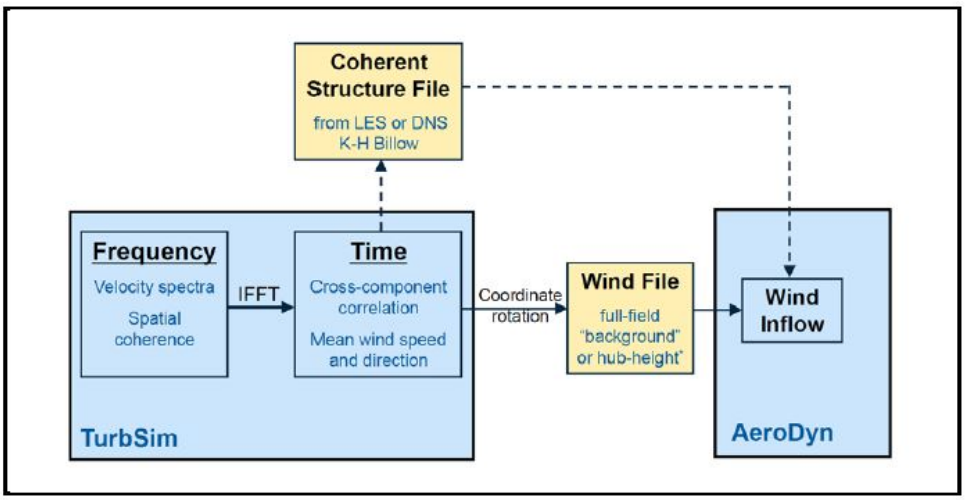

Figure 1.8: TurbSim simulation method.

SolidWorks

SolidWorks is a CAD software that was used to do a three-dimensional model of the floating platform, providing the total mass, mass moments of inertia and centre of mass to be used by OpenFAST and WAMIT.

Qblade

Qblade is an open-source software for wind turbine blade simulation a design. In this case, its functionalities were only used to upscale the discretized blades data to a 20Mw configuration. Although not used with that purpose, it is capable of simulating the dynamics of a wind turbine.

1.5 Objectives

The objectives of this master's thesis are:

- Implement a model of a 8MW wind turbine identical to the WindFloat project;
- Use that model to estimate the numerical accuracy of the OpenFAST simulations and establish the numerical settings for them;
- Scale the 8MW wind turbine to 20MW and analyse its behaviour;
- Provide an estimate of the LCOE for the 20MW wind turbine.

Chapter 2

Mathematical formulation

This chapter presents a summary of the theory behind the modules of the aero-hydro-servo-elastic code, OpenFAST. For logical reasons, the division is made according to the several modules. Their integration in the main is illustrated in figure 2.1.

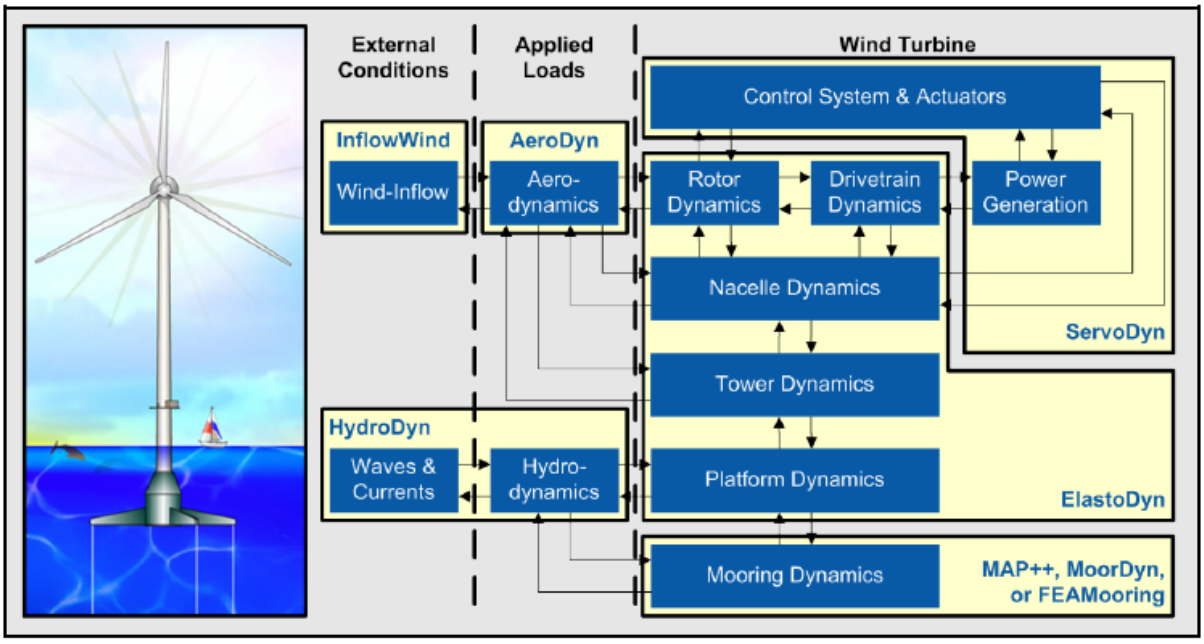

Figure 2.1: FAST's modules integration. [16]

2.1 Equation of motion (ElastoDyn)

As demonstrated by Jonkman [17], the complete non-linear equation of motion of the coupled wind turbine and floating platform system follows Newton's 2^{nd} law:

$$M_{ij}(q,u,t)\ddot{q}_j = f_i(q,\dot{q},u,t), \tag{2.1}$$

where M_{ij} is the (i, j) component of the inertia mass matrix, q corresponds to the degree of freedom, u is the set of control inputs, t is the time and $\ddot{q}$ the second time derivative of degree of freedom j. The force, f_i is a function that depends on the set of degrees of freedoms of the system, q, their first time derivatives, $\dot{q}$, on the set of control inputs, u and time, t. OpenFAST can model up to 24 degrees of freedom for a three-bladed floating wind turbine, not only the six shown in figure 2.2 [18].

$$M_{ij} = \begin{bmatrix} m & 0 & 0 & 0 & mz_g & -my_g \\ 0 & m & 0 & -mz_g & 0 & mx_g \\ 0 & 0 & m & my_g & -mx_g & 0 \\ 0 & -mz_g & my_g & I_x & -I_{xy} & -I_{xz} \\ -mz_g & 0 & -mx_g & -I_{yx} & I_y & -I_{yz} \\ -my_g & mx_g & 0 & -I_{zx} & -I_{zy} & I_z \end{bmatrix} \tag{2.2}$$

The form of the inertia mass-matrix is presented in equation (2.2) for a system with six degrees of freedom, like the floating platform [19].

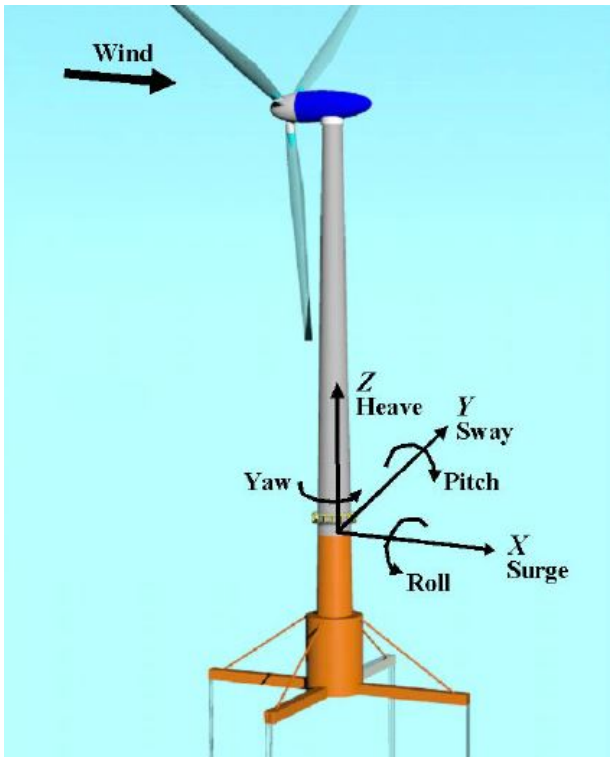

Figure 2.2: Floating platform degrees of freedom [20].

2.2 Hydrodynamic model (HydroDyn)

The hydrodynamic loading on the support platform of the wind turbine is of great importance and all the forces involved have to be taken into account. The total external load can be written as follows:

$$F_i^{Platform} = -A_{ij}\ddot{q}_j + F_i^{Hydro} + F_i^{Moorings}, \tag{2.3}$$

where A_{ij} is the infinite-frequency added mass, that summed with M_{ij} gives the total mass-matrix of the system. F_i^{Hydro} corresponds to the hydrodynamic load applied on the support platform and $F_i^{Moorings}$ is the contribution from the forces that the mooring lines apply on the platform. In the model used by OpenFAST, F_i^{Hydro} and $F_i^{Moorings}$ are included in the forcing function f_i from equation (2.1) [17]. In equation (2.3), i and j go from 1 to 6, the platform degrees of freedom (surge=1, sway=2, heave=3, roll=4, pitch=5, yaw=6).

The hydrodynamic loads are included in FAST through the HydroDyn module. These loads have contributions from inertia (added-mass), linear drag (radiation), incident-wave scattering (diffraction) and buoyancy (restoring). Sea current can be taken into account by HydroDyn too, but is not considered in this study.

The F_i^{Hydro} term from equation (2.3) has the following form:

$$F_i^{Hydro} = F_i^{Waves} + \rho g V_0 \delta_{i3} - C_{ij}^{Hydrostatics} q_j - \int_0^t K_{ij}(t-\tau)\dot{q}_j(\tau)d\tau \tag{2.4}$$

The force resulting from equation (2.4) has three different contributions. One from the first term, corresponding to the diffraction problem, another from the two following terms (hydrostatic problem) and a last one from the radiation problem. Overall, the hydrodynamic loads result from the integration of the pressure of the water over the wetted surface of the platform [20].

Throughout this work, second or higher order hydrodynamic effects are not accounted for. Also, translational displacements are considered to be small relative to the characteristic body length. Altogether, allows to use the simplest incident wave kinematics theory, Airy wave theory.

2.2.1 Diffraction problem

The diffraction problem has the purpose of determining the loads acting on a body fixed on its mean position. These loads emerge due to the scattering of incident surface waves.

HydroDyn represents irregular waves as a superposition of multiple wave components using the following equation for the wave elevation [20].

$$\zeta(t) = \frac{1}{2\pi}\int_{-\infty}^{\infty} W(\omega)\sqrt{2\pi S_\zeta^{2-sided}(\omega)}e^{j\omega t}d\omega \tag{2.5}$$

where where j is an imaginary number and ω is an individual wave frequency. $W(\omega)$ is the Fourier transform of a realization of a white Gaussian noise (WGN) time-series process with zero mean and unit variance and variance $\sigma^2 = \int_{-\infty}^{\infty} S_\zeta^{2-sided}(\omega)d\omega$. $S_\zeta^{2-sided}$ is the two-sided wave spectrum that can be calculated from the regular one-sided spectrum, $S_\zeta^{1-sided}$ found more commonly in ocean engineering. [17]

$$S_\zeta^{2-sided} = \begin{cases} \frac{1}{2}S_\zeta^{1-sided}(\omega) & \text{for } \omega \geq 0 \\ \frac{1}{2}S_\zeta^{1-sided}(-\omega) & \text{for } \omega < 0 \end{cases} \tag{2.6}$$

The one-sided spectrum used in this work was the JONSWAP spectrum and is detailed afterwards in

the section.

The excitation load on the support platform from incident waves is calculated including the term $X_i(\omega, \beta)$ in equation (2.5). It is a complex array that represents the wave-excitation force on the platform normalized per unit wave amplitude, where β is the wave propagation direction.

$$F_i^{Waves}(t) = \frac{1}{2\pi} \int_{-\infty}^{\infty} W(\omega) \sqrt{2\pi S_\zeta^{2-sided}(\omega)} X_i(\omega, \beta) e^{j\omega t} d\omega \tag{2.7}$$

The incident-wave-excitation force given by equation (2.7) is independent of the motion of the support platform, so the diffraction problem is independent from the radiation problem detailed in subsection 2.2.3.

JONSWAP spectrum

HydroDyn is able to simulate three types of wave spectrum: (1) Pierson-Moskowitz, (2) the Joint North Sea Wave Project (JONSWAP), both defined by the IEC 61400–3 [21] design standard, and (3) user-specified wave spectrum. In the course of this work, JONSWAP spectrum was the choice and it is defined in the code by its one-sided spectrum:

$$S_\zeta^{1-sided}(\omega) = \frac{1}{2\pi} \frac{5}{16} \left(\frac{\omega T_p}{2\pi}\right)^{-5} exp\left[-\frac{5}{4}\left(\frac{\omega T_p}{2\pi}\right)^{-4}\right] [1 - 0.287 \ln(\gamma)] \, \gamma^{exp\left\{0.5\left[\frac{\frac{\omega T_p}{2\pi} - 1}{\sigma(\omega)}\right]^2\right\}} \tag{2.8}$$

where H_s and T_p are the significant wave height and wave peak spectral period, respectively, both being user specified inputs. Also, $\sigma(\omega)$ is a scaling factor and γ is the peak shape parameter.

$$\sigma(\omega) = \begin{cases} 0.07 & \text{for } \omega \leq \frac{2\pi}{T_p} \\ 0.09 & \text{for } \omega > \frac{2\pi}{T_p} \end{cases} \tag{2.9}$$

$$\gamma = \begin{cases} 5 & \text{for } \frac{T_p}{\sqrt{H_s}} \leq 3.6 \\ exp\left(5.75 - 1.15 \frac{T_p}{\sqrt{H_s}}\right) & \text{for } 3.6 > \frac{2\pi}{T_p} \leq 5 \\ 1 & \text{for } \frac{T_p}{\sqrt{H_s}} > 5 \end{cases} \tag{2.10}$$

It is important to point out that if the peak shape parameter has a unit value, equation (2.8) corresponds to the Pierson-Moskowitz spectrum. This parameter can be changed in the HydroDyn input file, which by default will be equation (2.10), the JONSWAP spectrum. A comparison between these spectra is represented in figure 2.3.

2.2.2 Hydrostatic problem

The hydrostatic problem is simpler when compared with others in this section, but crucial for the behaviour of the floating structure. The load contribution from hydrostatics is represented by the second and third terms of equation (2.4).

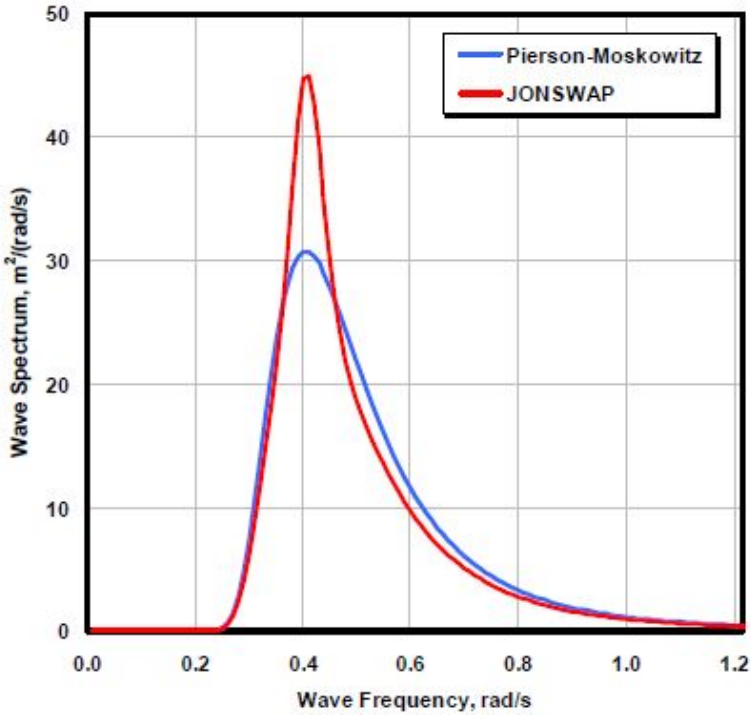

Figure 2.3: Pierson-Moskowitz and JONSWAP spectra comparison by Jonkman [17].

$$F^{Hydrostatics} = \rho g V_0 \delta_{i3} - C_{ij}^{Hydrostatics} q_j \tag{2.11}$$

The first term is the buoyancy force from the Arquimedes' principle, where ρ is the water density, g is the gravitational acceleration constant, V_0 is the volume of displaced water when the floating platform is in its undisplaced position and δ_{i3} is the $(i,3)$ component of the Kronecker-Delta function. The second term represents the changes in the hydrostatic force and moment that result from the effects of the water-plane area and the centre of buoyancy when there are changes in the support platform displacement, q_j. The hydrostatic restoring matrix is given by:

$$C_{ij} = \begin{bmatrix} 0 & 0 & 0 & 0 & 0 & 0 \\ 0 & 0 & 0 & 0 & 0 & 0 \\ 0 & 0 & \rho g A_0 & 0 & -\rho g \iint_{A_0} x\, dA & 0 \\ 0 & 0 & 0 & \rho g \iint_{A_0} y^2\, dA + \rho g V_0 z_{COB} & 0 & 0 \\ 0 & 0 & -\rho g \iint_{A_0} x\, dA & 0 & \rho g \iint_{A_0} x^2\, dA + \rho g V_0 z_{COB} & 0 \\ 0 & 0 & 0 & 0 & 0 & 0 \end{bmatrix} \tag{2.12}$$

where A_0 is the water-plane area when the platform is in its undisplaced position and z_{COB} is the vertical position of the COB. From equation (2.12) it is clear that hydrostatics provides restoring only in heave, roll and pitch [17].

2.2.3 Radiation problem

The radiation problem finds the loads acting on the floating platform when it moves without incident waves. When forced to oscillate, the body radiates waves, resulting in the radiation loads. The problem in this model is separated from the diffraction problem, meaning that the radiation loads will be independent of the incident waves. Hydrodynamic added-mass, A_{ij} and damping, B_{ij} are introduced in the model by OpenFAST's module HydroDyn after being calculated with WAMIT. The radiation problem corresponds to the last term of equation (2.4), a convolution integral:

$$F^{Radiation} = -\int_0^t K_{ij}(t-\tau)\dot{q}_j(\tau)d\tau \tag{2.13}$$

where K_{ij} is the (i,j) term of the wave-radiation-retardation kernel, t is the simulation time and τ is a user variable representing time. It represents the load contribution from wave radiation damping and also an additional contribution from added mass that depends on the frequency, that is not accounted for in equation 2.3 through A_{ij} [17]. In another words, the radiation kernel can be defined as an impulse-response function of the radiation problem.

2.3 Metacentric height

Due to the action of external forces on the floating platform, a heeling moment is created. As it leans to one side, the position of the centre of buoyancy will change from point B to B_1, as seen in figure 2.4. The trajectory that the change of the COB follows is assumed to be circular, with its centre lying in the metacentre, M. Since the centre of gravity, G is not aligned with B_1, a righting moment, M_R will arise to counter the instability introduced by the heeling moment. The distance GZ is called the "righting lever" [22] because it is the arm of the force that creates the righting moment. Thus, it can be calculated:

$$M_R = GZ \times \Delta \times g = GM \times \sin\theta \times \Delta \times g \tag{2.14}$$

where Δ is the water displacement and g the gravitational acceleration constant [23].

From ship stability theory, the stability of the a floating body can be divided in three categories according to the metacentric height, GM:

- $GM > 0$: stable;
- $GM = 0$: neutrally stable;
- $GM < 0$: unstable.

The metacentric height is:

$$GM = \frac{I}{\Delta} - GB \tag{2.15}$$

where I is the moment of inertia of the water-plane area and GB the distance between the centre of gravity and the COB (refer to figure 2.4 for graphic representation [22]) .

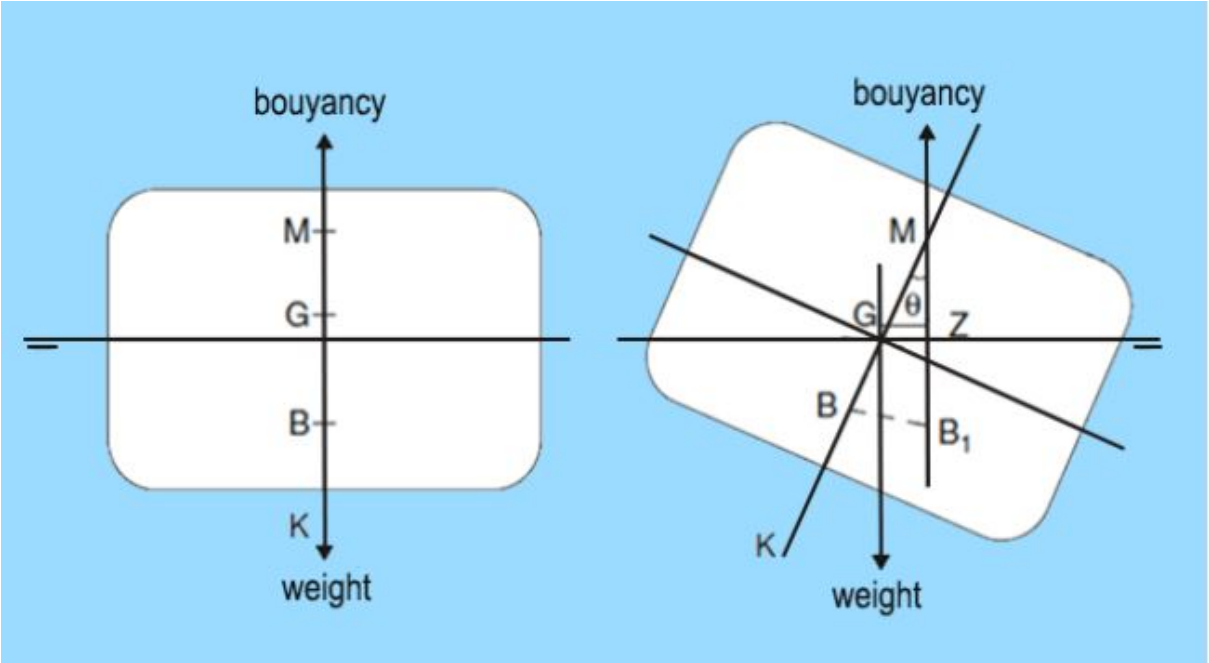

Figure 2.4: Stable equilibrium of a floating body.

For the case of a supporting platform of a wind turbine stability issues can not happen, so the meta-centre is always above the centre of gravity. In the operating states of a FOWT the stability in pitch is the most critical because of the moment created by the wind acting on the blades of the turbine.

2.4 Mooring system (MoorDyn)

The mooring system has the purpose of station-keeping of the FOWT and holding it against wind, waves and current. It consists of a number of cables connected to the fairleads of the floating platform and attached in the other end to an anchor. When the system changes position due to environmental loading, the tension of the mooring lines causes a restraining force on the fairlead connections that will keep the system in place. If this effect was assumed to be linear and damping ignored, the load from mooring lines, F_i^{Lines} on the platform would be given by:

$$F_i^{Lines} = F_i^{Lines,0} - C_{ij}^{Lines} q_j \tag{2.16}$$

where $F_i^{Lines,0}$ is the pre-tension of the mooring lines caused by the weight of the cable that is not resting on the seabed and C_{ij}^{Lines} is the linearised restoring matrix from all moorings. However, non-linearities will arise in the dynamic behaviour of the mooring system. So, the quasi-static model implemented in MoorDyn and coupled with OpenFAST, initially developed by Jonkman [17], takes into account the non-linear geometric restoration of the complete mooring system. This section presents a summary of how this is modelled into the code, through the main equations and assumptions used.

The user specifies the mooring layout, this means the fairlead and anchor positions relatively to the support platform and seabed, respectively. For each line, the unstretched length L, apparent weight in

fluid per unit length w, axial stiffness EA and coefficient of seabed static-friction drag C_B are also known properties. Knowing that the mooring line is submerged and buoyant one can calculate w:

$$w = \left(\mu_c - \rho\frac{\pi D_c^2}{4}\right) g \tag{2.17}$$

where μ_c is the mass of the line per unit length, ρ is the water density, D_c is the line diameter and g is the gravitational constant.

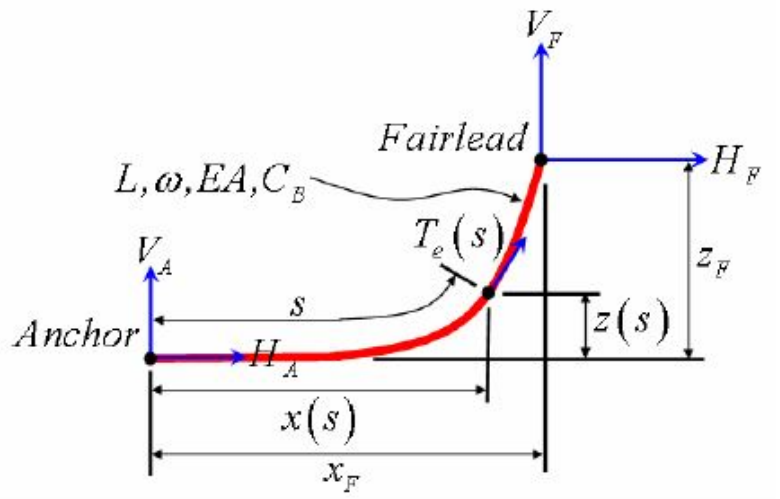

Figure 2.5: Local coordinate system for an individual mooring line.

When the module receives the fairlead positions (x_F, z_F) from an external code, first it transforms the coordinates from global frame to the local coordinate system represented in figure 2.5 [17]. In this referential, the fairlead coordinates are given by equation (2.18), where the horizontal and vertical components of the effective tension in the mooring line at the fairlead, H_F and V_F, are the unknowns. It is important to note that the following equation can only be used when part of the mooring line rests on the seabed. For the case where all the line is suspended more information can be found in [17], since this case is not under scrutiny in this work.

$$\begin{aligned} x_F\left(H_F, V_F\right) = L - \frac{V_F}{w} + \frac{H_F}{w}\ln\left[\frac{V_F}{H_F} + \sqrt{1+\left(\frac{V_F}{H_F}\right)^2}\right] + \frac{H_F L}{EA} \\ + \frac{C_B}{2EA}\left[-\left(L - \frac{V_F}{w}\right)^2 + \left(L - \frac{V_F}{w} - \frac{H_F}{C_B w}\right) MAX\left(L - \frac{V_F}{w} - \frac{H_F}{C_B w}, 0\right)\right] \end{aligned} \tag{2.18a}$$

$$z_F\left(H_F, V_F\right) = \frac{H_F}{w}\left[\sqrt{1+\left(\frac{V_F}{H_F}\right)^2} - \sqrt{1+\left(\frac{V_F - wL}{H_F}\right)^2}\right] + \frac{1}{EA}\left(V_F L - \frac{wL}{2}\right)^2 \tag{2.18b}$$

The first two terms in the right.hand side of equation (2.18a) represent the portion of the cable that rests on the seabed and the MAX function is needed in cases where the tension on the anchor is zero or different. If not zero, it means that the friction of the line with the seabed is not enough to overcome the

horizontal tension of the mooring line. If it is enough, the tension in the anchor will be zero.

Newton-Raphson iteration scheme is used to solve equations for H_F and V_F. The values from the previous time step are used as an initial guess for the following iteration. So, for the first time step, H_F^0 and V_F^0 are used as predictions [17].

$$H_F^0 = \left| \frac{w x_F}{2\lambda_0} \right| \tag{2.19a}$$

$$V_F^0 = \frac{w}{2} \left[\frac{z_F}{\tanh(\lambda_0)} + 1 \right] \tag{2.19b}$$

where λ_0 is a dimensionless catenary parameter depending on the initial configuration of the mooring line:

$$\lambda_0 = \begin{cases} 1 \times 10^6 & \text{for } x_F = 0 \\ 0.2 & \text{for } \sqrt{x_F^2 + z_F^2} \geq L \\ \sqrt{3\left(\frac{L^2 - z_F^2}{x_F^2} - 1\right)} & \text{otherwise} \end{cases} \tag{2.20}$$

Figure 2.6 presents a schematic summary of the procedure explained above, from the point where the position of the fairleads enters the module until it gives their updated value back to the external code.

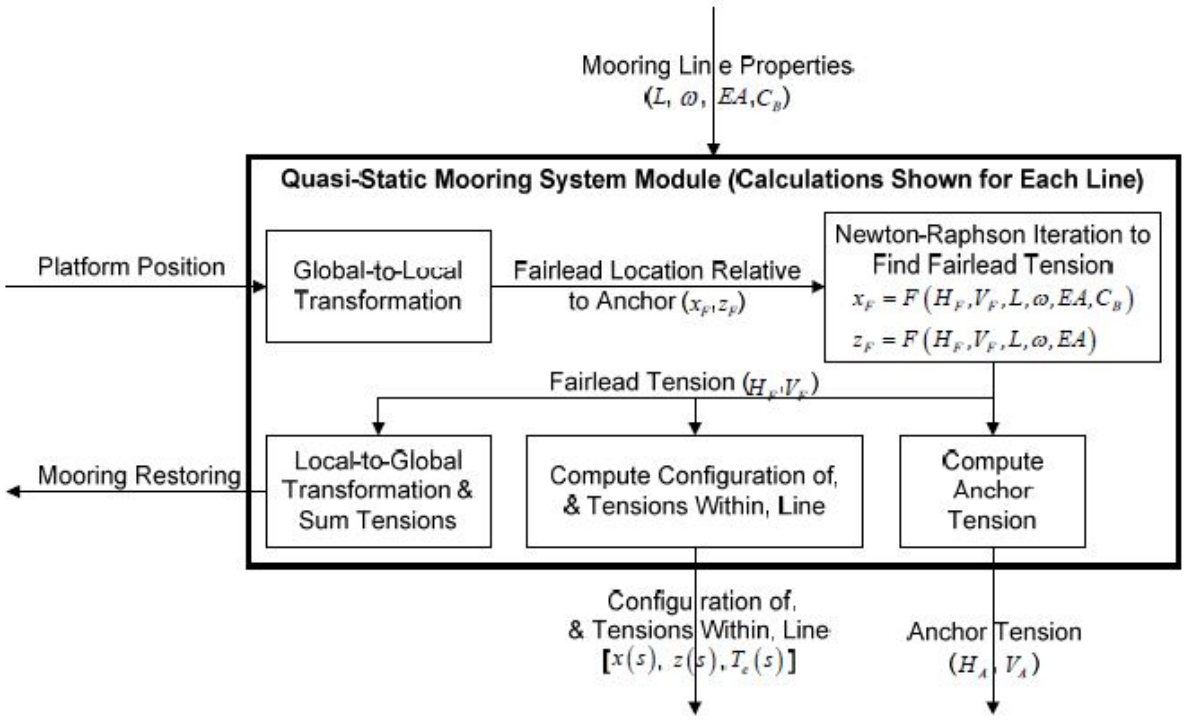

Figure 2.6: Summary of the mooring module developed by Jonkman [17].

2.5 Aerodynamic model (AeroDyn)

The changing aerodynamic forces acting on the wind turbine have to be calculated at each time step. To do so, OpenFAST calls AeroDyn that uses the blade element momentum theory to make the calculations.

2.5.1 Blade element momentum theory

Blade element momentum theory is a combination of blade element theory and momentum theory, as the name suggests. It assumes the blades are divided in several small elements. However, the following assumptions need to be taken into account when making the calculations for each element [24]:

- no interaction between annuli;
- in each element, the force of the flow acting on the blades is constant.

The rotating motion of these elements will trace out the annular rings seen in figure 2.7. The sum of the forces in each element along the span of the blade give the total forces and moments acting on the turbine [25].

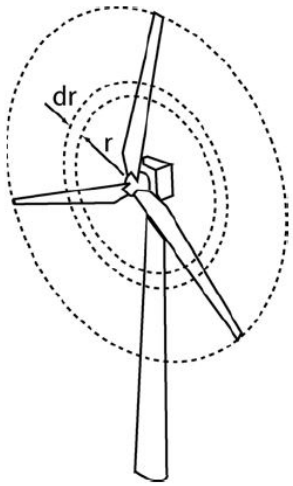

Figure 2.7: Annular ring, dr in the rotor plane.

The equations of thrust and torque for the annular ring shown in figure 2.7 can be written in the following way according to the momentum theory:

$$dT = 4\pi r \rho U_{\infty}^2 (1-a) a dr \tag{2.21}$$

$$dQ = 4\pi r^3 \rho U_{\infty} \Omega (1-a) a' dr \tag{2.22}$$

The forces acting on an airfoil are represented in figure 2.8. Also, what is mentioned as V_{Total}, is the inflow velocity and has contributions from wind, the velocity of the rotating blade and induced axial and tangential velocity. The angle ϕ is the sum of the angles of attack and pitch of the blade, r is the radial position on the blade, Ω is the angular rotation, a is the axial induction factor, a' is the rotational induction

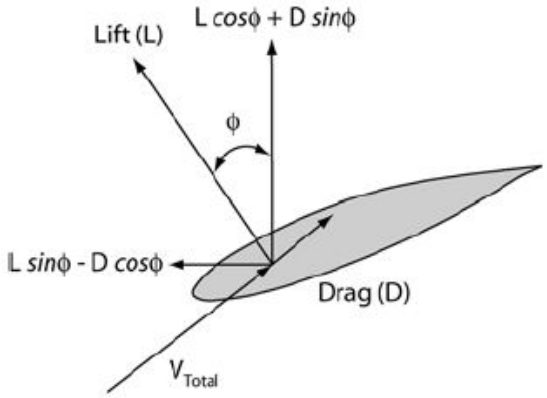

Figure 2.8: Aerodynamic forces acting on an airfoil section from the rotor plane.

factor and ρ is the air density. Making the trigonometric relations between the mentioned quantities, the following relationships can be established.

$$dT = B(L\cos\phi + D\sin\phi)dr \tag{2.23}$$

$$dQ = B(L\sin\phi - D\cos\phi)rdr \tag{2.24}$$

where B is the number of blades, L is the lift of the blade and D is drag.

Knowing the following expressions for C_n and the solidity ratio, σ, one can combine equations (2.21) and (2.23) to calculate the axial induction factor, a:

$$C_n = C_l\cos\phi + C_d\sin\phi \tag{2.25}$$

$$\sigma = \frac{Bc}{2\pi r} \tag{2.26}$$

$$a = \left[1 + \frac{4\sin^2\phi}{\sigma C_n}\right]^{-1} \tag{2.27}$$

The same can be done for the rotational induction factor, a', but now combining equations (2.22) and (2.24).

$$C_t = C_l\sin\phi - C_d\cos\phi \tag{2.28}$$

$$a' = \left[1 + \frac{4\sin\phi\cos\phi}{\sigma C_t}\right]^{-1} \tag{2.29}$$

AeroDyn implements an iterative scheme to find the values of axial induction factor, a and rotational induction factor, a', that can be summarized in the following steps [24]:

1. guess starting values for a and a';
2. calculate ϕ, C_l and C_d;
3. update a and a';
4. check for convergence and repeat if it does not satisfy the convergence criteria.

2.5.2 Prandtl tip and hub-loss model

Tip and hub-loss models are introduced because the original blade element momentum theory is unable to take into account the effect of vortices shed from the blade tips and from near the hub into the wake on the induced velocity field.

$$F = \frac{2}{\pi} \cos^{-1} e^{-} f \tag{2.30a}$$

$$f = \frac{B}{2} \left(\frac{R - r}{r \sin \phi} \right) \tag{2.30b}$$

Here, R corresponds to the blade radius. The correction factor, F just has to be multiplied by equations (2.21) and (2.22). Modelling the hub-loss is similar, equation (2.30b) just has to be replaced by:

$$f = \frac{B}{2} \left(\frac{r - R_{hub}}{R_{hub} \sin \phi} \right) \tag{2.31}$$

For elements where the aerodynamics are affected by both models, the corrections factors are multiplied and introduced in equations (2.21) and (2.22). [25]

2.5.3 Glauert correction

BEM theory is not valid for $a > 0.5$. For this values of the induction factor the flow in the wake starts to propagate upstream, violating its basic principles. In other words, the wind velocity in the far wake would be negative. Physically this is impossible, so it has to be corrected in the theory. Buhl Jr [26] derived a modification for Glauert's empirical relation that included the tip-loss correction:

$$C_T = \frac{8}{9} + \left(4F - \frac{40}{9} \right) a + \left(\frac{50}{9} - 4F \right) a^2 \tag{2.32}$$

that solved for the induction factor is:

$$a = \frac{18F - 20 - 3\sqrt{C_T \left(50 - 36F\right) + 12F \left(3F - 4\right)}}{36F - 50} \tag{2.33}$$

Chapter 3

8MW model description

The starting point for this work is the implementation of the 8MW model in OpenFAST. The objective is to replicate the Vestas V164-8.0MW wind turbine, which is used in the Windfloat Atlantic project. So, everything needs to be modelled, from the blades of the turbine to the mooring system of the floating platform that supports it. Table 3.1 presents a general list of characteristics of the turbine and figure 3.1 its power curve.

Table 3.1: Vestas V164-8.0MW wind turbine general properties [27].

Rated electrical power	8 MW
Rotor orientation, Configuration	Upwind, 3 blades
Control	Variable speed; Collective pitch
Cut-in wind speed	4 m/s
Cut-out wind speed	25 m/s
Rated wind speed	13 m/s
Rotor diameter	164 m
Hub diameter	4 m
Hub height	101.75 m
Cut-in, Rated rotor speed	4.8, 10.5 rpm
Rated generator speed	500 rpm

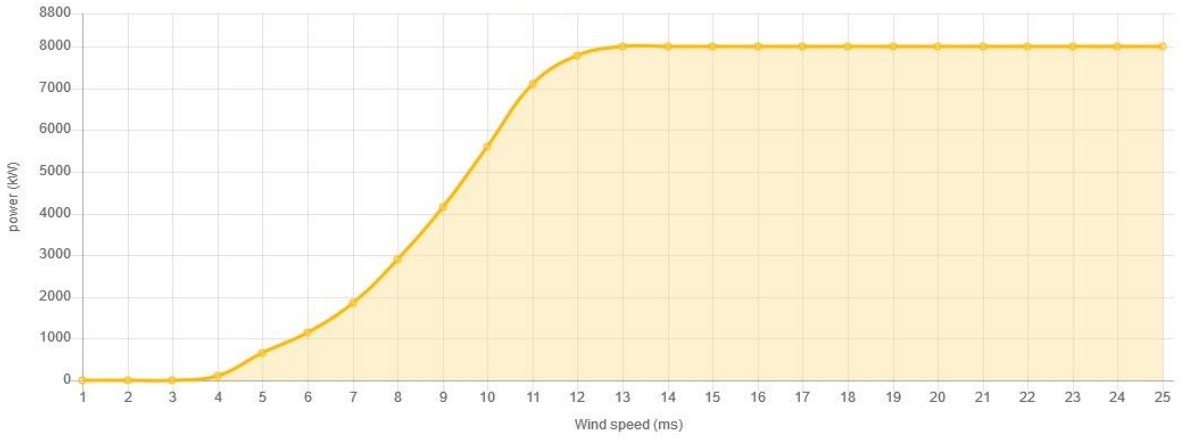

Figure 3.1: Power curve of the wind turbine [28].

This chapter presents an explanation on how the several components of the platform were implemented in OpenFAST and how the most important inputs for the code were calculated. All the inputs files were adapted from the 5MW baseline library that NREL provides together with the code. These files are the result of an extensive verification made for the OC3 and OC4 projects. For this case, the input files were specifically adapted from the semi-submersible floating platform study, which corresponds to the second phase of the OC4 project. [29]

It should be noted that there is no section dedicated to the blade pitch control system, because doing extensive research on control methods is out of the scope of this work. So, it was opted to keep the control method from NREL's 5MW baseline wind turbine with just a few changes to suit the new model. Moreover, nacelle yaw control is shut off, since all the test cases done in the course of the project have wind aligned with the turbine.

3.1 Nacelle and tower

Going through the nacelle first, the most important data as inputs for code implementation are the mass and dimensions. According to the manufacturer [27], the dimensions are displayed in figure 3.2 and it has a mass of 390 tonnes.

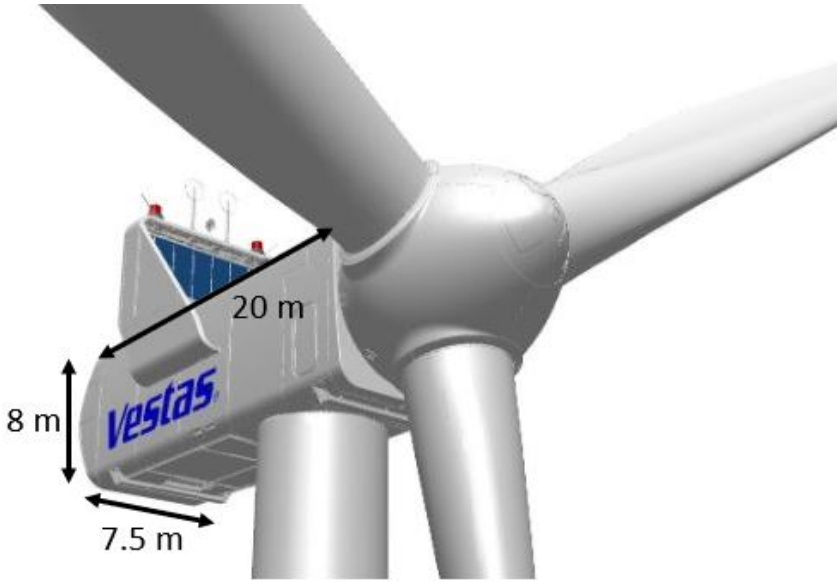

Figure 3.2: Nacelle dimensions (modiffied from [30]).

The tower diameter and thickness used were based on the work developed by Desmond et al. [31], whereas the mass density was calculated by multiplying the cross sectional area by the equivalent density of the structure. The value used for it is higher than the steel density to account for some secondary structures that may be present, in this case 8500 kg/m^3. Table 3.2 presents the data that OpenFAST, through the ElastoDyn and Aerodyn modules, requires to model the tower.

For a tower length of 87.35 meters, this gives a tower mass of $4.35 \times 10^5\ kg$.

Table 3.2: Tower properties.

Height (m)	Diameter (m)	Thickness (m)	Mass density (kg/m)
11.90	7.70	0.0360	7367.61
21.04	7.43	0.0346	6832.92
29.73	7.16	0.0332	6318.32
38.42	6.89	0.0318	5823.79
47.11	6.62	0.0304	5349.36
55.80	6.35	0.0290	4895.00
64.49	6.08	0.0276	4460.73
73.18	5.81	0.0262	4046.54
81.87	5.54	0.0248	3652.43
90.56	5.27	0.0234	3278.41
99.25	5.00	0.0220	2924.46

3.2 Rotor blades and hub

There is limited information given by the manufacturer about the blade data of the V164-8.0MW wind turbine, which means that a few assumptions need to be made. The data gathered about the blades is presented in table 3.3 [27].

Table 3.3: Blade data from manufacturer.

Rotor diameter (m)	164.0
Blade length (m)	80.0
Hub radius (m)	2.0
Maximum chord (m)	5.4

It is important to note that information regarding blade and hub weight is available, but with the assumptions that are made bellow, those values stop being valid for this case. Also, the hub radius is determined knowing the rotor diameter and the blade length.

The chord at the root and tip of the blade result from an interpolation between the NREL 5MW baseline [32] and the 10MW DTU reference wind turbine [33]. The location of the maximum chord length in the blade is kept the same, in terms of percentage of its length, as in the 5MW baseline. The values between the maximum chord location and the root and tip follow a linear trend, an increase from root to maximum chord and a decrease from there to the tip. However, there are two exceptions, since the first and last two nodes have the same chord to be coherent with the DTU reference. Blade twist and airfoil distribution are kept the same from the 5MW baseline model developed by Jonkman et al. [32].

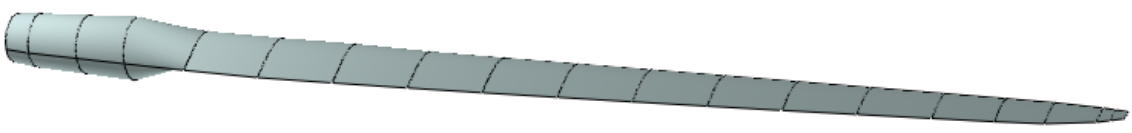

Figure 3.3: Blade of the 8MW wind turbine (20 nodes).

Table 3.4: Blade characteristic data for input files.

Span (m)	Chord (m)	Twist ($^\circ$)	Airfoil
0.00	4.65	13.31	1
2.00	4.65	13.31	1
6.47	4.83	13.31	1
10.94	5.02	13.31	2
15.41	5.21	13.31	3
19.88	5.40	11.48	4
24.35	5.18	10.16	4
28.82	4.97	9.01	5
33.29	4.75	7.80	6
37.76	4.53	6.54	6
42.23	4.32	5.36	7
46.71	4.10	4.19	7
51.18	3.88	3.13	8
55.65	3.67	2.32	8
60.12	3.45	1.53	8
64.59	3.23	0.86	8
69.06	3.02	0.57	8
73.53	2.80	0.37	8
78.00	2.17	0.11	8
80.00	2.17	0.11	8

Table 3.5: Correspondence between airfoils and their numbering.

Numbering	Airfoil
1	Cylinder 1
2	Cylinder 2
3	DU40
4	DU35
5	DU30
6	DU25
7	DU21
8	NACA64

Table 3.4 presents the most important inputs for the OpenFAST's modules, AeroDyn and ElastoDyn, while table 3.5 shows the airfoil numbering used by the code. The choice of having the blade discretized in 20 nodes is explained in chapter 4. Figure 3.3 is the representation of one blade of the wind turbine generated by Qblade.

It is important to note that the mass per length of the blade was taken from the DTU 10MW reference wind turbine as an initial guess. This is seen as a conservative approach, since the wind turbine modelled in this case has a smaller rating. In spite of that, the blade mass that resulted from the initial approach is very similar to the weight given by the manufacturer. Consulting the manufacturer [27], one can see that the blade weight is 35 000 kg, which is close to the one calculated by ElastoDyn shown in table 3.6. For this reason, it was opted to keep the mass per length initially guessed.

Table 3.6: Mass of rotor components.

Component	Mass (kg)
Hub	90 000
Blade	36 699.37
Rotor	200 098.11

3.3 Floating platform

The floating platform consists in three columns placed in the vertices of an equilateral triangle, each with a hexagonal heave plate on the bottom end and with the tower placed on one fo the columns. Also, there are several braces connecting the main columns that are not modelled neither in the WAMIT simulations nor in OpenFAST, because their diameter is small when compared with the main columns. Thus, it will not have an impact on the hydrodynamics of the model, since only potential theory is used. To get more accurate results on the forces acting on the smaller structures, one should complement the model with the use of the Morrison equation, which is out of the scope of this work. These braces also have an important role on the structural integrity of the floating platform, however, in this project, it is considered to be undeformable, so there is no need to take it into account. Figure 3.4 is an illustration of WindFloat's floating platform.

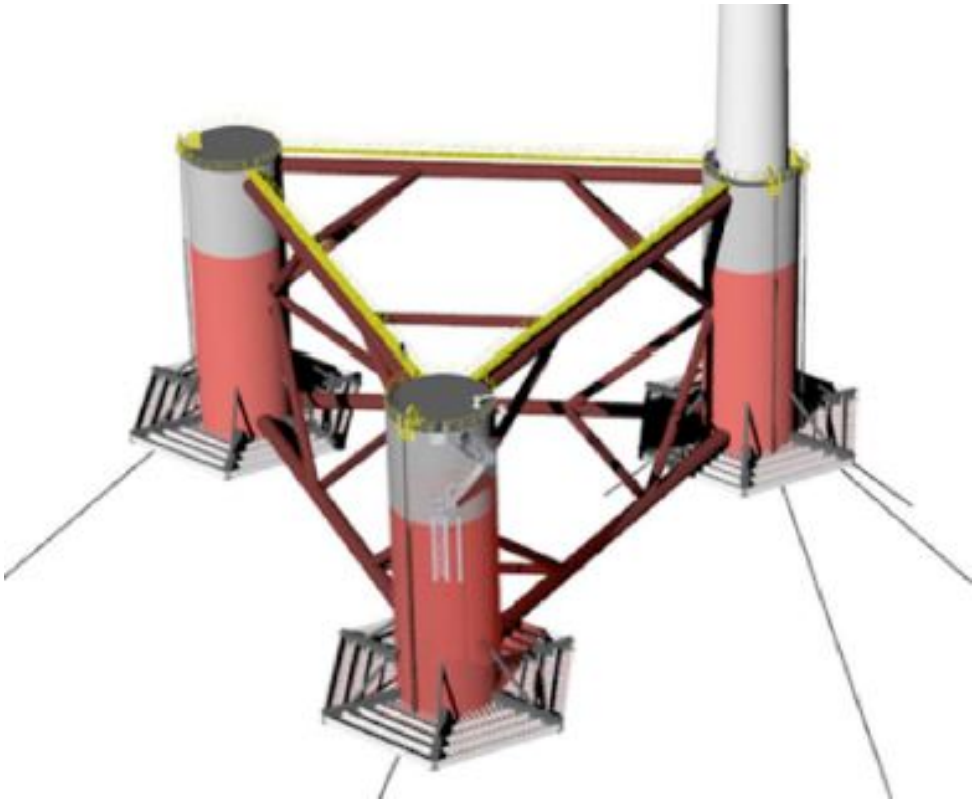

Figure 3.4: Three-dimensional view of the Windfloat support structure. [34]

Moreover, the main dimensions of the floating structure can be observed in figures 3.5 and 3.6.

Table 3.7 has also the dimensions of the floating platform that were used as an input for OpenFAST's

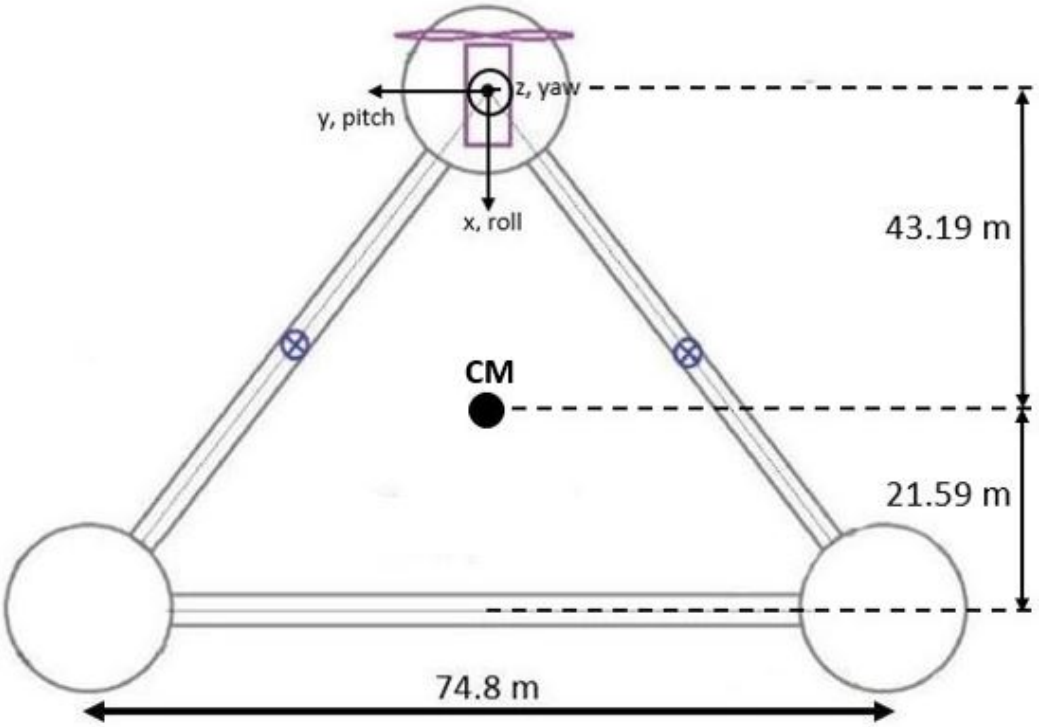

Figure 3.5: Top view of the floating platform without heave plates (modified from [35]).

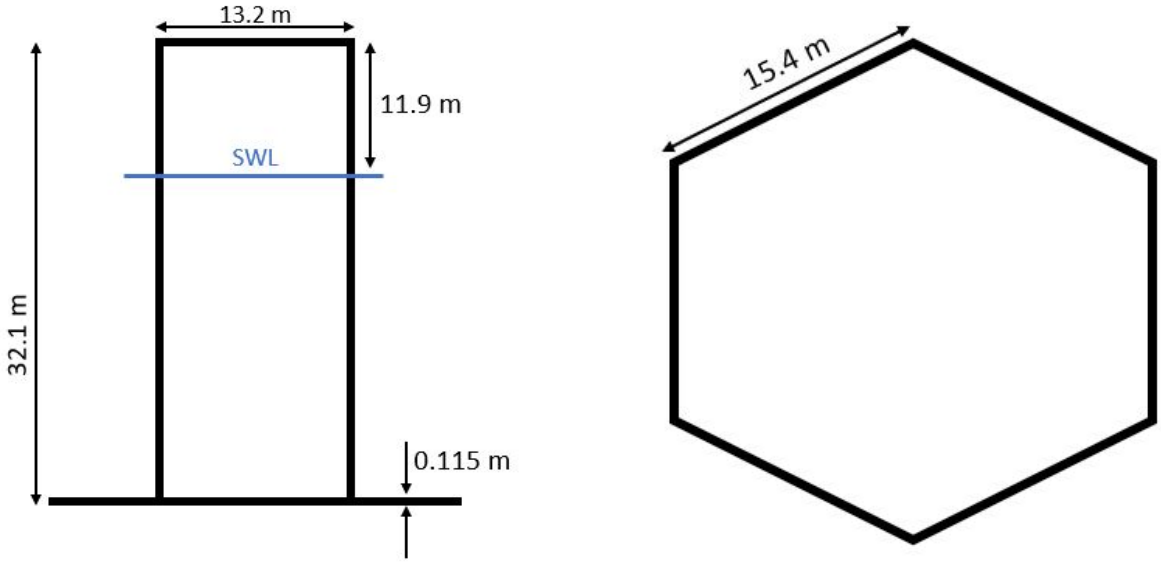

(a) Column (b) Heave plate

Figure 3.6: Side view of the column and top view of the heave plate.

modules HydroDyn and ElastoDyn, but also to make a CAD model of the platform in SolidWorks. The CAD model was used to get the mass and moments of inertia of the platform, that are essential for the code to simulate the motion of the system.

To balance the moment crated by the wind turbine (sitting in a column, not in the platform CM) and in order to keep the operating draft (equal weight and buoyancy) as designed, the columns of the platform

Table 3.7: Floating platform properties for the 8MW wind turbine.

Operating draft	32.1	$[m]$
Column elevation over sea level	11.9	$[m]$
Column centre to centre	74.8	$[m]$
Column diameter	13.2	$[m]$
Length of heave plate edge	15.4	$[m]$
Heave plate thickness	0.115	$[m]$
Column thickness	0.0320	$[m]$
Mass (no ballast)	2.62450E+06	$[kg]$
Ballast water (column 1)	5976	$[m^3]$
Ballast water (columns 2 and 3)	3488	$[m^3]$
Roll inertia	3.18392E+09	$[kgm^2]$
Pitch inertia	3.18392E+09	$[kgm^2]$
Yaw inertia	5.30743E+09	$[kgm^2]$

are filled with ballast water. The process to find the amount of ballast needed is divided in two steps, first to ensure stability and a second to keep the draft.

Firstly, the water in columns 2 and 3 need to balance the moment created by the wind turbine structure located on column 1. Checking the dimensions of the platform in figure 3.5, one can do the balance of moments considering the weight of each column and of the wind turbine to get the weight of the ballast inside columns 2 and 3.

$$\begin{aligned}(2W^{Column} + 2W_{2,3}^{Ballast}) \times d =& (W^{Turbine+tower} + W^{Column}) \times 2d \\ \Rightarrow W_{2,3}^{Ballast} =& W^{Turbine+tower}\end{aligned} \tag{3.1}$$

where W^{Column} is the weight of the column (steel), $W_{2,3}^{Ballast}$ is the weight of ballast water needed in columns 2 and 3, $W^{Turbine+tower}$ is the wind turbine plus tower weight and $d = 21.59m$.

Then, the impulse, B generated by the submerged part of the platform is calculated knowing the displaced fluid, $V^{Displaced}$, the water density, ρ and the gravitational constant is g.

$$B = \rho g V^{Displaced} \tag{3.2}$$

$$W^{Turbine+tower} + 3W^{Column} + 2W_{2,3}^{Ballast} + 3W_{1,2,3}^{Ballast} = B \tag{3.3}$$

Equation (3.3) gives the ballast weight for column 1 and the extra amount of ballast to add in columns 2 and 3.

To conclude,

- Column 1 ballast: $W_{1,2,3}^{Ballast}$
- Column 2 ballast: $W_{1,2,3}^{Ballast} + W_{2,3}^{Ballast}$
- Column 3 ballast: $W_{1,2,3}^{Ballast} + W_{2,3}^{Ballast}$

$$V = \frac{\frac{W}{g}}{\rho} \tag{3.4}$$

To get the volume of water needed in each column, the only step is to use equation (3.4), knowing that the water density is $\rho = 1025\ kg/m^3$ and the gravitational constant is $g = 9.81\ m/s^2$.

3.4 Mooring system

The floating platform is secured by three catenary mooring lines that are spread symmetrically about the platform centre of mass. The fairleads, where the moorings are connected to the platform, are located above the heave plate, while the anchors are located at a depth of 100 meters in a radius of 600 meters from the platform centre of mass. One line is directed along the negative x-axis and the others are distributed uniformly along the platform, in such way that there is a 120° angle between them as seen in figure 3.7.

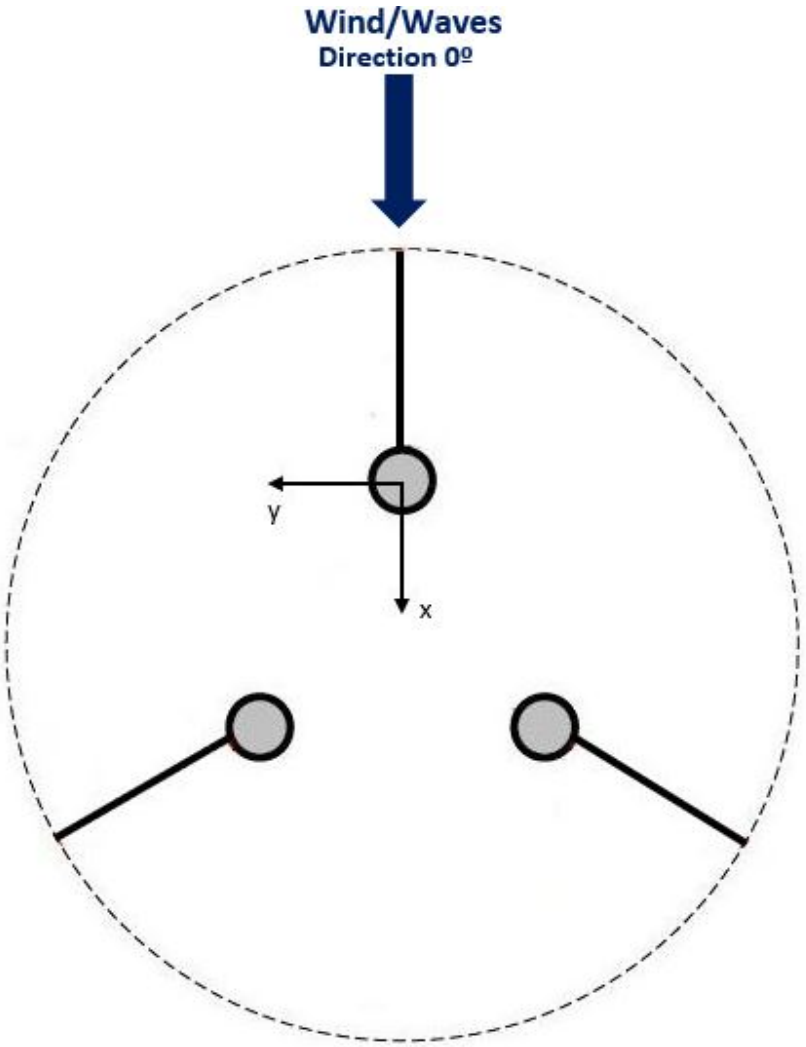

Figure 3.7: Sketch of the mooring system (not at scale).

Tables 3.8 and 3.9 have all the data needed by OpenFAST's module, MoorDyn, to model the mooring

system.

Table 3.8: Mooring configuration.

Number of mooring lines	3	[-]
Angle between adjacent mooring lines	120	[$^\circ$]
Water depth	100	[m]
Depth from fairlead to seabed	68.015	[m]
Radius to anchors from platform CM	600	[m]
Radius to fairleads from platform CM	43.18	[m]
Unstretched mooring line length	566	[m]

Although most of the mooring lines used in ocean engineering have multiple segments made of a combination of different materials (rope, chain or wires), the code can only model homogenous lines. Thus, the properties observed in table 3.9 are the equivalent properties of the mooring line used. [17]

Table 3.9: Mooring line properties.

Diameter	0.076	[m]
Mass per unit length	113.35	[kg/m]
Axial stiffness	7.536E+09	[N]
Transverse added mass coefficient	0.8	[-]
Tangential added mass coefficient	0.25	[-]
Transverse drag coefficient	2.0	[-]
Tangential drag coefficient	0.4	[-]

Chapter 4

Numerical convergence properties

Most of the the mathematical models used in engineering do not have an analytical solution, this means that numerical solutions are required. OpenFAST is the code used to address this problem. As in all numerical solutions, it is not exact and there will be an error.

$$e(\phi_i) = \phi_i - \phi_{exact} \tag{4.1}$$

There are three types of errors that appear when determining the numerical solution of a model [36].

Round-off error

The round-off error is a consequence of the limited precision of the machine in use. In this case, double precision is adopted to avoid round-off errors.

Iteration error

Most mathematical models have non-linear equations that are discretized, resulting in a system of linear equations that is often solved using iterative methods. As a result, this error can only be reduced until the machine precision.

Discretization error

The discretization error results from the transformation of differential or integral equations into an algebraic system of equations. When compared to the other sources of numerical error already mentioned, the discretization error is usually dominant and has a tendency to decrease as the number of degrees of freedom of the system increases. Since the exact solution of the problem in hand is unknown, the discretization error is determined using mesh/time refining studies. In this case, instead of the mesh, it is the time step of the code that is being refined. It is important to mention that each individual OpenFAST's module can run with a different time step from the glue code. In spite of this fact, the time step is kept the same for all modules in every simulation, with the exception of the mooring module, MoorDyn, that has to run with a time step one hundred times smaller.

4.1 Numerical convergence

The goal of doing the verification of this code is to prove that the solution it provides does not contain significant errors. Since the discretization error is dominant, that will be the focus of this study. The goal here is get an estimate of the discretization error of a solution by successively reducing the time step. The solution at time step i is:

$$\phi_i = \phi_0 + \alpha h_i^p \tag{4.2}$$

And the error estimate for time step i is:

$$e = \phi_i - \phi_0 = \alpha h_i^p \tag{4.3}$$

where ϕ_i is the approximate solution for a given time step, ϕ_0 is the estimated value of the exact solution for the smallest time step used in the study, α is a constant and p is the observed order of convergence [36]. In a normal mesh refinement study, h_i would be the size of the mesh, but in this case is the size of the time step.

Another purpose of this work is to prove that p will be equal to the theoretical order of convergence of the discretized equations. In the mesh refining study, the time step is reduced by half at each iteration, from $\Delta t = 0.1s$ until $\Delta t = 0.003125s$.

Table 4.1: Time steps used in the simulations.

i	Δt $[s]$
6	0.1
5	0.05
4	0.025
3	0.0125
2	0.00625
1	0.003125

So as to calculate the order of convergence and the discretization error at leat three different time steps are needed. This means that, with the six time steps used, four orders of convergence and discretization errors can be found, one for each set of three time steps. The equations presented bellow were applied to the four sets of three time steps seen in table 4.2.

Table 4.2: Sets of time steps used to calculate the discretization error.

Set	1	2	3	4
i	6-5-4	5-4-3	4-3-2	3-2-1

It should be noted that the indices of the variables in the equations presented bellow range from 1 to 3, which does not correspond to the numbering of the indices from table 4.1, but rather a numbering within each set of three time steps.

$$\phi_3 - \phi_2 = \alpha h_2^p \left(\left(\frac{h_3}{h_2} \right)^p - 1 \right) \tag{4.4}$$

$$\phi_2 - \phi_1 = \alpha h_1^p \left(\left(\frac{h_2}{h_1} \right)^p - 1 \right) \tag{4.5}$$

$$\phi_1 - \phi_0 = \alpha h_1^p \tag{4.6}$$

The order of convergence is calculated by dividing equation (4.4) by (4.5). After doing some algebraic manipulation and knowing that $\frac{h_3}{h_2} = \frac{h_2}{h_1} = 2$ one gets:

$$p = \frac{\ln\left(\frac{\phi_3 - \phi_2}{\phi_2 - \phi_1} \right)}{\ln(2)} \tag{4.7}$$

Since the exact solution, ϕ_0 is unknown, to get the discretization error, equation (4.5) is divided by (4.6).

$$e_1 = \phi_1 - \phi_0 = \frac{\phi_2 - \phi_1}{2^p - 1} \tag{4.8}$$

Once this is known, an estimate for the exact value of a variable can be calculated rearranging equation (4.8).

$$\phi_0 = \phi_1 - \frac{\phi_2 - \phi_1}{2^p - 1} \tag{4.9}$$

The error presented in tables 4.4, 4.6 and 4.8 is determined as a percentage of the estimate of the exact solution calculated with the three lowest time step.

The first step towards finding the time step size at which the problem has converged was to simplify the system. The model of a floating wind turbine is complex and OpenFAST makes discretization not only in time, but also in space. As seen in chapter 2, AeroDyn discretizes the turbine blades to implement the BEM theory, moreover, MoorDyn code also discretizes the mooring lines in several segments to calculate the fairlead positions and tensions. Therefore, the system was simulated for 300 seconds with the aerodynamic module disabled, with just irregular waves with a peak period, T_p of 10 seconds and a significant wave height, Hs of 2.5 meters. Before completing this step, it was verified that having the mooring lines divided in 40 segments or more was enough for it to not have an influence in the time step convergence study.

To start, the aerodynamic module was disabled and there is no wind, so the only external forces acting on the FOWT come from the waves. Since the platform is symmetrical and the waves are aligned with the axis of symmetry, no motion is expected to arise in sway, roll and yaw. Thus, the first convergence study is done analysing only the solutions for surge, heave and pitch. This way, the time step can be chosen without influence of the spatial discretization of the blades. The following tables are a compact summary of the results obtained with the six time steps used in the simulations.

Table 4.3: Mean surge, heave and pitch for each time step.

Mean			
Δt (s)	Surge (m)	Heave (m)	Pitch $(^\circ)$
0.1	0.00949	0.00143	-0.03562
0.05	-0.00162	0.00125	-0.03555
0.025	-0.00986	0.00114	-0.03547
0.0125	-0.01496	0.00108	-0.03542
0.00625	-0.01774	0.00104	-0.03539
0.003125	-0.01924	0.00103	-0.03538

Table 4.4: Order of convergence, estimate of exact solution and discretization error for surge, heave and pitch based on the mean values.

	Surge				Heave				Pitch			
i	$\phi_i - \phi_{i-1}$	p	ϕ_0	$e_i(\%)$	$\phi_i - \phi_{i-1}$	p	ϕ_0	$e_i(\%)$	$\phi_i - \phi_{i-1}$	p	ϕ_0	$e_i(\%)$
6	1.111E-02				1.830E-04				-7.233E-05			
5	8.248E-03	0.43	-0.03364		1.089E-04	0.75	0.00098		-8.383E-05	-0.21	-0.03608	
4	5.097E-03	0.69	-0.02321	113.01	6.225E-05	0.81	0.00099	15.92	-5.172E-05	0.70	-0.03533	-1.73
3	2.774E-03	0.88	-0.02105	39.20	3.340E-05	0.90	0.00101	8.26	-2.378E-05	1.12	-0.03537	0.24
2	1.507E-03	0.88	-0.02103	15.75	1.800E-05	0.89	0.00101	3.85	-1.391E-05	0.77	-0.03536	0.06
1				8.52				2.09				0.06

Table 4.5: RMS surge, heave and pitch for each time step.

RMS			
Δt (s)	Surge (m)	Heave (m)	Pitch $(^\circ)$
0.1	0.59998	0.12889	0.13400
0.05	0.68291	0.12855	0.14294
0.025	0.73875	0.12889	0.14942
0.0125	0.77102	0.12910	0.15314
0.00625	0.78819	0.12920	0.15509
0.003125	0.79742	0.12925	0.15614

Table 4.6: Order of convergence, estimate of exact solution and discretization error for surge, heave and pitch based on the RMS values.

	Surge				Heave				Pitch			
i	$\phi_i - \phi_{i-1}$	p	ϕ_0	$e_i(\%)$	$\phi_i - \phi_{i-1}$	p	ϕ_0	$e_i(\%)$	$\phi_i - \phi_{i-1}$	p	ϕ_0	$e_i(\%)$
6	-8.293E-02				3.404E-04				-8.935E-03			
5	-5.585E-02	0.57	0.85391		-3.436E-04	-0.01	0.098258		6.483E-03	0.46	0.16656	
4	-3.226E-02	0.79	0.81516	14.25	-2.095E-04	0.71	0.12943	-28.08	-3.724E-03	0.80	0.15817	10.89
3	1.717E-02	0.91	0.80773	5.46	-1.032E-04	1.02	0.12930	0.25	-1.950E-03	0.93	0.15724	3.19
2	-9.233E-03	0.90	0.80816	2.42	-5.133E-05	1.01	0.12931	0.08	-1.051E-03	0.89	0.15737	1.36
1				1.33				0.04				0.78

The non-linear equations of motion are solved integrating in time using the 4^{th} order Runge-Kutta method. This is one of the three methods that the user can choose explicitly in OpenFAST. If no further investigation was to be done, one should expect that the order of convergence of the solutions would be close to four. Although, it does not happen, as seen in tables 4.4, 4.6 and 4.8, the order of convergence

Table 4.7: Maximum surge, heave and pitch for each time step.

Maximum			
Δt (s)	Surge (m)	Heave (m)	Pitch $(^\circ)$
0.1	1.61701	0.27633	0.23021
0.05	1.64900	0.27681	0.25578
0.025	1.66621	0.27731	0.27410
0.0125	1.67504	0.27742	0.28420
0.00625	1.68004	0.27740	0.28922
0.003125	1.68200	0.27740	0.29190

Table 4.8: Order of convergence, estimate of exact solution and discretization error for surge, heave and pitch based on the maximum values.

	Surge				Heave				Pitch			
i	$\phi_i - \phi_{i-1}$	p	ϕ_0	$e_i(\%)$	$\phi_i - \phi_{i-1}$	p	ϕ_0	$e_i(\%)$	$\phi_i - \phi_{i-1}$	p	ϕ_0	$e_i(\%)$
6	-3.199E-02				-4.753E-04				-2.556E-02			
5	-1.720E-02	0.90	1.68622		-4.992E-04	-0.07	0.26689		-1.832E-02	0.48	0.32044	
4	-8.836E-03	0.96	1.68437	1.19	-1.152E-04	2.12	0.27746	-3.76	-1.010E-02	0.86	0.29663	15.71
3	-5.000E-03	0.82	1.68656	0.55	2.193E-05	2.39	0.27740	0.01	-5.017E-03	1.01	0.29417	4.21
2	-1.958E-03	1.35	1.68326	0.39	2.401E-06	3.19	0.27740	0.00	2.681E-03	0.90	0.29498	1.68
1				0.07				0.00				1.04

of the several solutions tends to a value close to one. The explanation for this lies in the way that the code is implicitly discretizing the radiation equation (2.13) with the rectangle rule, which is a first order method.

$$F^{Rad} = -\Delta t_{Rad} \sum_{i=n-N_{Rad}}^{n-1} K_{n-i-1}\dot{q}_i \tag{4.10}$$

This equation has the particularity of being discretized only considering a specific amount of time history N_{Rad}, that can be chosen by the user, in this case it is considered to be 60 seconds. This is enough for the radiation impulse response functions to decay to near-zero as demonstrated by Duarte et al. [37].

Analysing the results gathered above, one can conclude that a reasonable time step to use in the simulations to do throughout this work is 0.00625 seconds. In terms of RMS, the biggest error is for the solution in surge of 2.42% and 15.75% for the mean value. The support platform of the wind turbine does not provide restoring in surge by itself, it is the mooring lines that keep it stable when there is a displacement along the x-axis. Since there are more factors influencing the dynamics related with surge, such has the spatial discretization of the mooring lines already mentioned above, one would expect that this was where the most significant errors would emerge.

The reason to choose this time step instead of the smallest, and consequently the one with the smaller error, lies on the fact that the simulations would become too heavy in computational terms and that would consume too much time. As a consequence, opting for the non optimal solution, but one that gives confidence in the results is a compromise that has to be done.

Afterwards, the aerodynamic module was enabled. The wave conditions are kept the same as before

and a wind profile with a mean speed of $13m/s$ was generated by TurbSim.

The goal now is to find the ideal number of nodes per blade of the rotor that allow the BEM method to converge. For this, a total of nine simulations were done. Firstly, with 10 nodes per blade, three simulations with the three smaller time steps considered before. Then, the procedure was repeated for 20 and 40 nodes per blade. This allows to determine the discretization error that would be obtained for different number of nodes used.

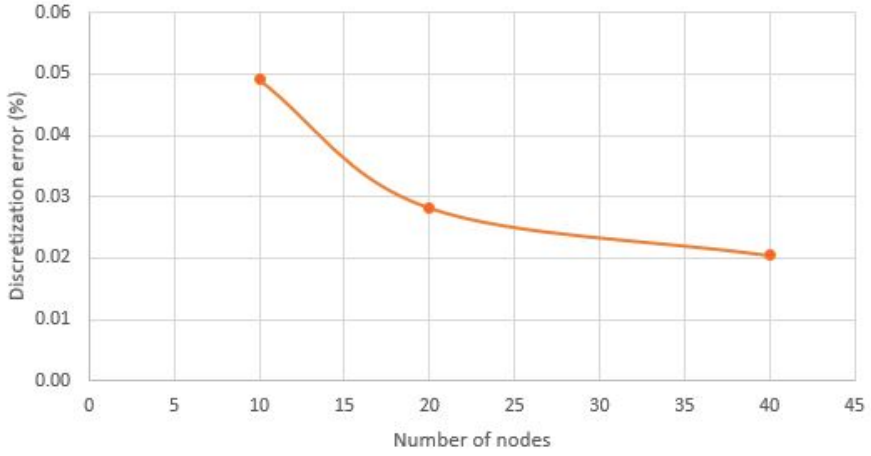

(a) Pitch

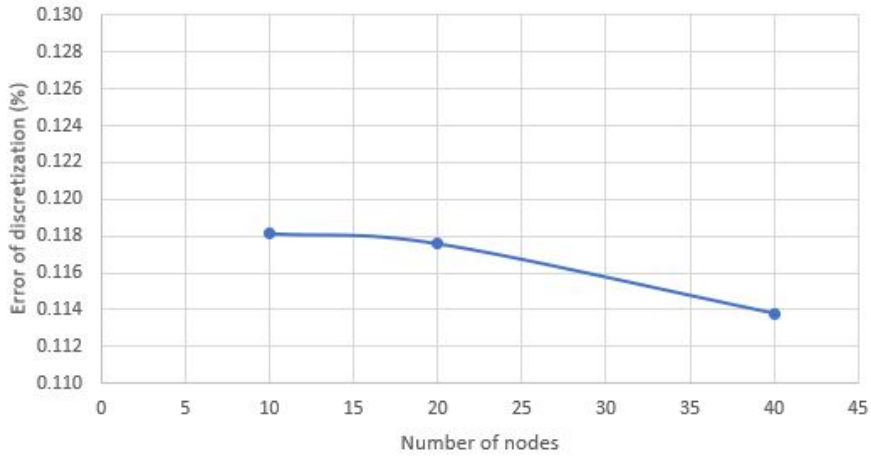

(b) Heave

Figure 4.1: Error of discretization in function of the number of nodes per blade.

When analysing a FOWT in a situation with wind aligned with the axis of symmetry of the support platform and perpendicular to the rotor, the most important degree of freedom to look upon is pitch. Also, it is the one where the number of nodes used by AeroDyn shown the biggest influence. From figure 4.1,for the case of pitch, one can observe that the error of discretization is decreasing when the number of nodes per blade increases. Although the error is already very small when using 10 nodes, it is clear that there is a significant decrease when going from 10 to 20 nodes, being 57% of the error for 10 nodes, and a smaller decrease from 20 to 40 nodes. In the latter, the error of discretization is 42% of the initial error with 10 nodes.

The same trend can be seen for the heave case, but with the difference that the error changes very

little with the increasing number of nodes. With 40 nodes the error is 89% of the error with 10 nodes. So, one can confirm that the convergence of the number of nodes for the BEM method has little influence on the heave solution, the reduction in terms of error is small when using finer spatial discretization.

Even though the optimal solution would be to choose 40 nodes per blade, as demonstrated, it was opted to use only 20. This comes from weighting time of simulation against accuracy of the results. The decrease in error obtained using 40 nodes does not make up for the time saved by using only 20. This is because the largest decrease in error arises from 10 to 20 rather than from 20 to 40.

4.2 Statistical convergence

Achieving statistical convergence means that, at some point in time, the initial conditions of a simulation stop having influence over the solution in analysis. In order to do that, a very large simulation is needed, so that by the end of that period of simulated time there is no influence of the initial conditions.

In this case, a time of 2500 seconds was simulated and values of the relevant solutions were taken in periods of 500 seconds from that time series. To have consistent results, the outer factors that will have an influence on the floating structure need to be the same in each period of 500 seconds. Thus, the wave spectrum and the wind profile have to be periodic, like shown by figure 4.2. In it is represented the time between 2000 and 2500 seconds, which corresponds to a period that repeats itself every 500 seconds.

At tables 4.9 and 4.11 the mean values and RMS were taken, respectively, for every period. Tables 4.10 and 4.12 display the difference in percentage between the result taken in one period and the result of the last (2000-2500s). That is, the smaller this percentage, the less influence the initial condition still has on the solutions taken in this period.

Table 4.9: Mean values in each period for the selected variables.

Mean							
Period (s)	Surge (m)	Sway (m)	Heave (m)	Roll ($^\circ$)	Pitch ($^\circ$)	Yaw ($^\circ$)	Rotation Speed (rpm)
0-500	3.830	-0.456	-0.059	-0.046	3.144	0.549	10.56
500-1000	4.706	-0.411	-0.091	0.095	3.244	0.334	10.49
1000-1500	4.734	-0.449	-0.092	0.089	3.239	0.349	10.49
1500-2000	4.729	-0.474	-0.092	0.071	3.236	0.380	10.49
2000-2500	4.731	-0.481	-0.092	0.066	3.240	0.390	10.49

Table 4.10: Error of the mean value in each period when compared with the last $500s$ (zero influence of initial conditions).

Mean							
Period (s)	Surge	Sway	Heave	Roll	Pitch	Yaw	Rotation Speed
0-500	19.04%	5.38%	35.53%	170.08%	2.95%	-40.91%	-0.70%
500-1000	0.55%	14.55%	1.67%	-44.53%	-0.15%	14.34%	0.01%
1000-1500	-0.06%	6.77%	-0.26%	-35.15%	0.01%	10.38%	-0.01%
1500-2000	0.05%	1.50%	-0.11%	-8.66%	0.10%	2.42%	0.00 %
2000-2500	0.00%	0.00%	0.00%	0.00%	0.00%	0.00%	0.00%

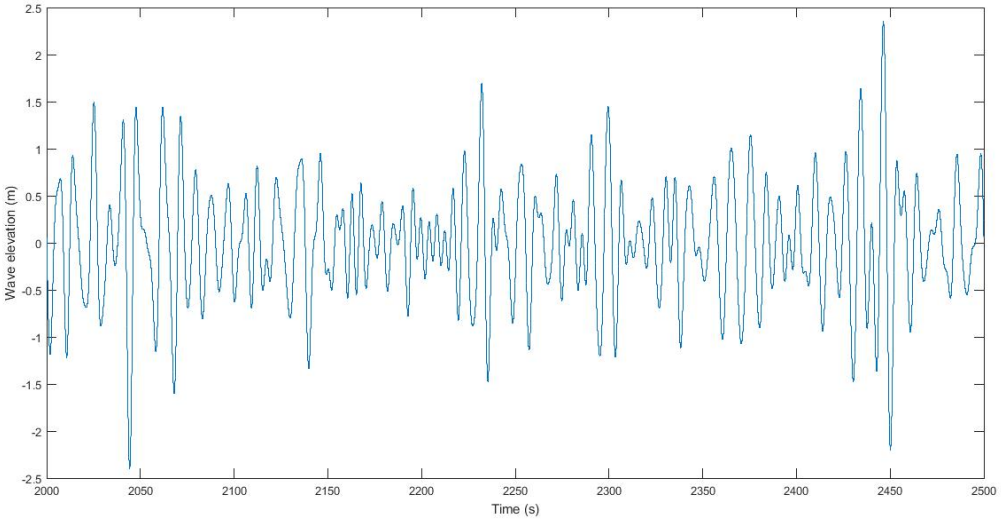

(a) $H_s = 2.5m; T_p = 10s$

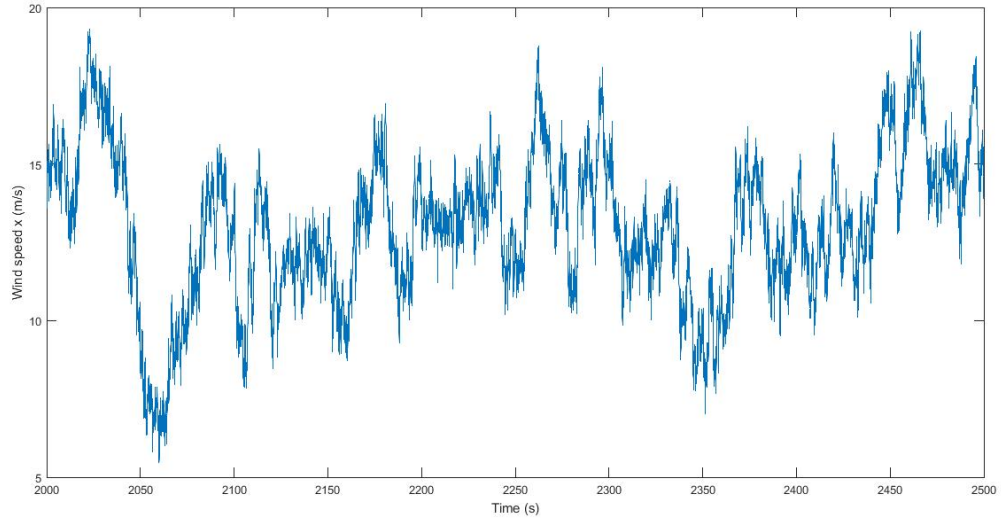

(b) Mean wind speed: $13m/s$

Figure 4.2: Wave spectrum and wind profile plots.

Table 4.11: RMS values in each period for the selected variables.

RMS							
Period (s)	Surge (m)	Sway (m)	Heave (m)	Roll ($^\circ$)	Pitch ($^\circ$)	Yaw ($^\circ$)	Rotation Speed (rpm)
0-500	4.120	1.011	0.203	1.186	3.441	1.941	10.67
500-1000	4.753	1.412	0.216	1.724	3.366	2.763	10.54
1000-1500	4.779	1.594	0.209	1.927	3.361	3.113	10.55
1500-2000	4.774	1.600	0.207	1.922	3.359	3.114	10.54
2000-2500	4.777	1.576	0.204	1.888	3.363	3.061	10.54

Looking into tables 4.10 and 4.12, one can see that the first period must be ruled out when taking the results from a simulation because the influence of the initial conditions is still significant. Ideally, the results would be taken from 1500 seconds, since the difference for every solution is bellow 5%, with the

Table 4.12: Error of the RMS value in each period when compared with the last $500s$ (zero influence of initial conditions).

RMS							
Period (s)	Surge	Sway	Heave	Roll	Pitch	Yaw	Rotation Speed
0-500	13.75%	35.82%	0.47%	37.19%	-2.32%	36.59%	-1.22%
500-1000	0.51%	10.39%	-5.93%	8.7%	-0.09%	9.76%	0.01%
1000-1500	-0.05%	-1.17%	-2.40%	-2.09%	0.06%	-1.70%	0.00%
1500-2000	0.06%	-1.54%	-1.58%	-1.81%	0.10%	-1.73%	0.00%
2000-2500	0.00%	0.00%	0.00%	0.00%	0.00%	0.00%	0.00%

exception of the mean roll, which still is less than 9%.

However, it would not be feasible to do so, because removing the first 1500 seconds implies making a simulation of at least 2000 seconds. In fact, to have 2000 seconds of simulated time, means a simulation of about 7200 seconds of real time, that is two hours per simulation. For the next part of this work, several load cases of wind and wave conditions are tested and spending two hours in each of them is not possible. So, once again, a compromise is done. Looking at the results presented, it was opted to make simulations of 1000 seconds and take out the first 500 seconds. Consequently, the period of simulation used to take results will be from 500 to 1000 seconds, where the difference for the last period is less than 10% for every solution, with the exceptions of mean and RMS sway and mean roll and yaw. Although all of them being above 10%, the only one and that is significantly bigger is mean of roll and that is not the most important motion in scope of this work.

Chapter 5

Upscaling to 20MW

The scaling procedure of the 20MW wind turbine results from the application of classical similarity rules between it and the 8MW wind turbine described in chapter 3. These rules are based on the assumption of geometrical similarities between both turbines. In other words, this means that if the power output of the wind turbine is 2.5 times bigger (from 8 to 20MW), the rotor swept area is also 2.5 times bigger than before. So, the scaling factor will be:

$$sf = \sqrt{\frac{20}{8}} \simeq 1.58. \tag{5.1}$$

This results in the scaling factors for the rotor and tower presented in table 5.1. The upscaling procedure is defined in more detail in [33].

Table 5.1: Scaling factors for rotor and tower parameters.

Design parameter	Scaling factor
Linear dimensions (diameter, maximum chord, tower thickness, etc)	sf
Power	sf^2
Thrust at rated wind	sf^2
Rotor mass	sf^3
Moment of inertia of the blade	sf^5

Regarding the floating platform and hydrodynamic forces acting upon it, the same geometric scaling factor from equation (5.1) is used. Taking the moment of inertia of the platform as an example, all the scaling parameters in table 5.2 were derived as follows:

$$I = mr^2 \tag{5.2}$$

This equation can be written in a dimensional form as

$$[I] = [mass] \times [length]^2, \tag{5.3}$$

from this, one can get the derived scaling factor, Λ for the inertia, because the mass is scaled by a factor of sf^3 and radius by sf. Therefore, one can write:

$$\Lambda = sf^3 \times sf^2 = sf^5 \tag{5.4}$$

Table 5.2: Scaling factors for the floating platform.

Design parameter	Scaling factor
Linear dimensions (diameter and height of columns, plate thickness, etc)	sf
Mass	sf^3
Moment of inertia	sf^5
Force	sf^3

Another similarity factor needs to be accounted for when handling the rotational characteristics of the wind turbine. To ensure these characteristics are the same, the tip-speed ratio, TSR needs to be maintained constant. [38]

$$TSR = \frac{\Omega R}{V} \tag{5.5}$$

In equation (5.5), Ω corresponds to the rotational speed of the rotor, R its radius and V the wind velocity acting on the turbine.

As this model does not take into account any physical limitations, there may be risks related with mechanical fractures, aeroelastic instabilities and buckling. Besides, there may be case-specific constraints related with the deployment site, like noise or height limitations. As a consequence, each real wind turbine will deviate from the theoretical model.

A summary of the most general characteristics of the 20MW wind turbine are presented in table 5.3.

Table 5.3: 20MW wind turbine general properties.

Rated electrical power	20 MW
Rotor orientation, Configuration	Upwind, 3 blades
Control	Variable speed; Collective pitch
Cut-in wind speed	4 m/s
Cut-out wind speed	25 m/s
Rated wind speed	13 m/s
Rotor diameter	259.3 m
Hub diameter	6.32 m
Hub height	159.43 m
Rated rotor speed	6.64 rpm
Rated generator speed	500 rpm

5.1 Upscaled inputs for OpenFAST

The implementation of the 20MW model is similar to that presented in chapter 3. All the data used for the modules' input files is presented in this section. The majority of it was scaled according to the methodology described and any exception is stated. Also, it is important to note that some parameters are simply ignored, because they have no influence over the solution being studied.

5.1.1 Nacelle and tower

Tables 5.4 and 5.5 present all the data necessary regarding the tower and nacelle needed to run a simulation. Note that the inertia of the nacelle about the yaw axis is omitted because rotations of the nacelle about that axis are not enabled in the scope of this work.

Table 5.4: Nacelle properties.

Length (m)	31.6
Width (m)	11.9
Height (m)	12.6
Weight (kg)	1 541 610

Table 5.5: Tower properties.

Height (m)	Diameter (m)	Thickness (m)	Mass density (kg/m)
18.82	12.17	0.0569	18419.0
33.27	11.75	0.0547	17082.3
47.01	11.32	0.0525	15795.8
60.75	10.89	0.0503	14559.5
74.49	10.47	0.0481	13373.4
88.23	10.04	0.0459	12237.5
101.97	9.61	0.0436	11151.8
115.71	9.19	0.0414	10116.3
129.45	8.76	0.0392	9131.1
143.19	8.33	0.0370	8196.0
156.93	7.91	0.0348	7311.2

5.1.2 Rotor blades and hub

The procedure to get the upscaled blade data was different from the other parts of the turbine. Instead of upscaling each parameter individually from the 8MW model, it was opted to use Qblade software. NREL's 5MW reference blade data comes with the code and giving the hub radius, blade length and root chord, all presented in table 5.6, it calculates all the discretized data needed for OpenFAST's input files.

All the necessary parameters for the input files related with the hub and rotor blades are presented in table 5.7. The airfoil numbering is the same as in the 8MW model and can be observed in table 3.5.

Table 5.6: Upscaled rotor data.

Rotor diameter (m)	259.31
Blade length (m)	126.49
Hub radius (m)	3.61
Maximum chord (m)	7.36
Root chord (m)	5.06

Table 5.7: Blade characteristic data for input files.

Span (m)	Chord (m)	Twist ($^\circ$)	Airfoil
0.00	5.06	13.08	1
2.73	5.60	13.08	1
8.36	6.09	13.08	1
13.98	6.59	13.08	2
21.02	7.19	13.08	3
29.46	7.36	11.48	4
37.90	7.05	10.16	4
46.33	6.72	9.01	5
54.77	6.34	7.80	6
63.21	5.93	6.54	6
71.65	5.54	5.36	7
80.08	5.15	4.19	7
88.52	4.76	3.13	8
96.96	4.37	2.32	8
105.40	3.98	1.53	8
112.43	3.66	0.86	8
118.05	3.30	0.37	8
123.67	2.21	0.16	8
125.08	1.66	0.08	8
126.49	1.11	0.00	8

5.1.3 Floating platform

The floating platform geometry is kept the same as in the 8MW model. So, all the assumptions apply to this case. The only difference is that the new data is upscaled with the methodology already presented in this chapter. Also, the same calculations are done to get the amount of ballast water in each column. Thus, figures 3.5 and 3.6 stay relevant for the 20MW model, the only difference being the dimensions of the structure. All the data necessary to introduce in the input files related with the floating platform is presented in table 5.8.

5.1.4 Mooring system

Regarding the mooring system, there are some inputs that remain the same from the 8MW model, since the mooring configuration is kept. However, the parameters regarding the platform dimensions change and also the anchor radius and unstretched mooring line length were scaled according with sf. All the parameters regarding the mooring configuration are shown in table 5.9.

Table 5.8: Floating platform properties for the 20MW wind turbine.

Operating draft	50.75	$[m]$
Column elevation over sea level	18.82	$[m]$
Column centre to centre	118.27	$[m]$
Column diameter	20.87	$[m]$
Length of heave plate edge	24.35	$[m]$
Heave plate thickness	0.182	$[m]$
Column thickness	0.032	$[m]$
Mass (no ballast)	7.80750E+06	$[kg]$
Ballast water (column 1)	12 085	$[m^3]$
Ballast water (columns 2 and 3)	15 031	$[m^3]$
Roll inertia	3.16474E+10	$[kgm^2]$
Pitch inertia	3.16474E+10	$[kgm^2]$
Yaw inertia	5.27183E+10	$[kgm^2]$

Table 5.9: Mooring configuration.

Number of mooring lines	3	[-]
Angle between adjacent mooring lines	120	$[^\circ]$
Water depth	100	$[m]$
Depth from fairlead to seabed	49.432	$[m]$
Radius to anchors from platform CM	880.39	$[m]$
Radius to fairleads from platform CM	68.28	$[m]$
Unstretched mooring line length	895	$[m]$

Since the mooring system design is not the main focus of this project, although it has an important role on the platform's dynamic behaviour, it was opted to only scale the line diameter, keeping the other properties the same. The reason for this assumption was that scaling both the diameter and the mass per length with this methodology would result in an over-prediction of the total mass of the moorings.

5.2 Hydrostatic stability and free decay

Before testing how the system reacts to the forces of nature, wind and waves in this case, since the presence of current is neglected, three free decay tests are done. It consists in evaluating the system's response to an initial offset from the equilibrium position.

To create the conditions mentioned above, the "still water" flag is enabled in HydroDyn and "still air" is activated in InflowWind. Also, to make sure that no aerodynamic effects are account for, AeroDyn module is disabled in OpenFAST. Then, three simulations of 1000 seconds are done. First, making a 5 meter displacement in surge, then 2 meters in heave and, lastly, 2 degrees in pitch.

Also, note that before making this procedure, several tests were run in order to validate trimming and integrity of the inputs. [39]

The decaying motion of the platform is recorded as a time series, from which one can calculate the logarithmic decrement, δ

$$\delta = \frac{1}{n} \ln \frac{x_0}{x_n} \tag{5.6}$$

Taking δ from equation (5.6), the damping ratio, ζ can be calculated with equation (5.7)

$$\zeta = \frac{1}{\sqrt{1 + (\frac{2\pi}{\delta})^2}} \tag{5.7}$$

Finally, the damping ratio is used to calculate the damped period of oscillation, T_d, from which the natural period, T_n is easily defined.

$$T_d = \frac{2\pi}{\omega_d} = \frac{2\pi}{\omega_n \sqrt{1-\zeta^2}} = \frac{T_n}{\sqrt{1-\zeta^2}} = \frac{t_n - t_0}{n} \tag{5.8}$$

$$T_n = T_d \sqrt{1-\zeta^2} \tag{5.9}$$

The platform response in decay can be observed from figure 5.1 to 5.3.

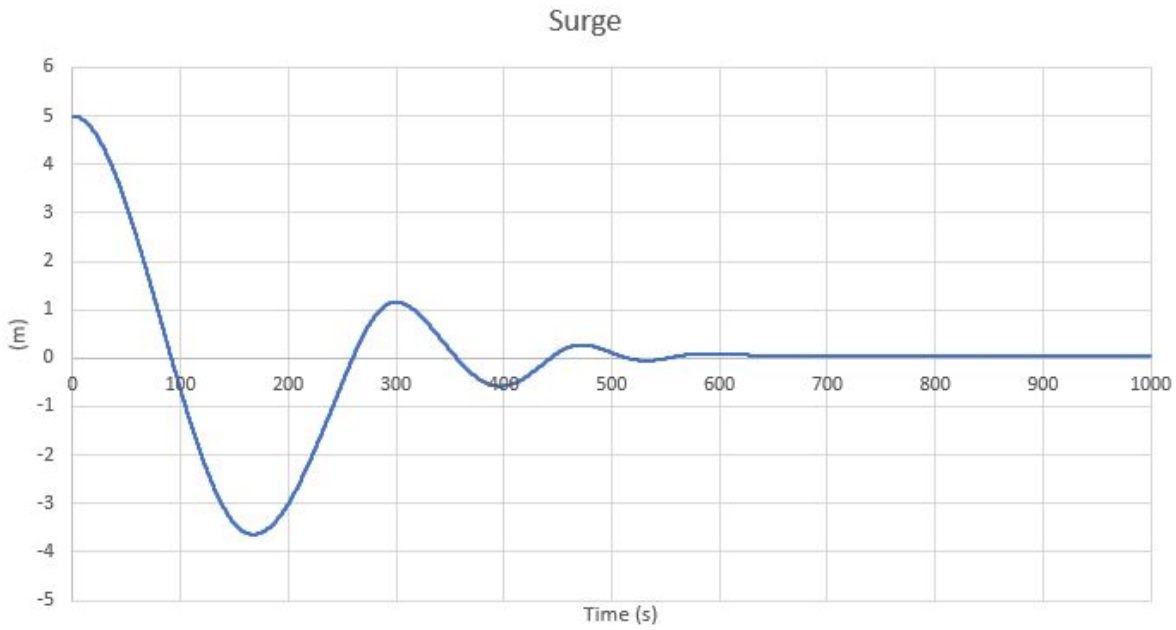

Figure 5.1: Surge motion for free decay load case.

Regarding the restoring in surge, it is difficult to draw a conclusion regarding the stability of the platform, since this degree of freedom depends heavily on the configuration of the mooring system.

As heave is regarded, one can easily see that the motion is very little damped, and the same occurs with pitch. The fact that the effect of viscous forces is not being modelled may be causing this phenomenon. Following the methodology done by Robertson et al. [29], for models that use potential theory without Morison elements, like this one, need extra damping to accurately represent the system's real damping. It is possible to include this extra damping coefficients trough the "additional quadratic drag" matrix in HydroDyn and they are estimated for the semi-submersible platform from OC4. However, to

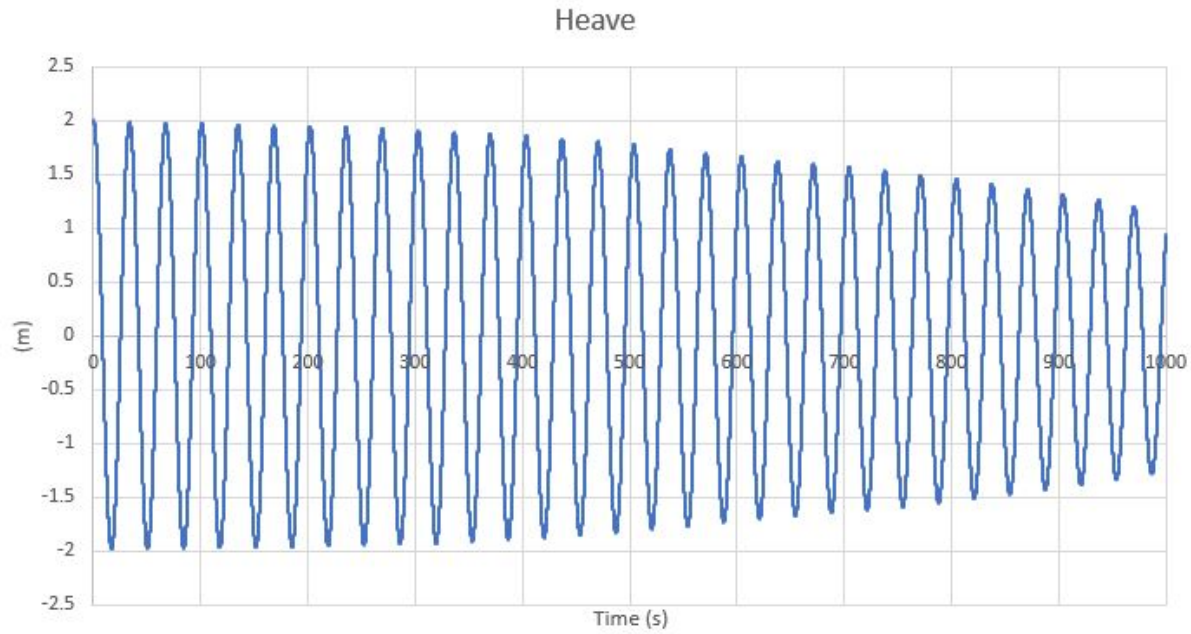

Figure 5.2: Heave motion for free decay load case.

scale them accurately for this model is difficult due to the differences in the two geometries.

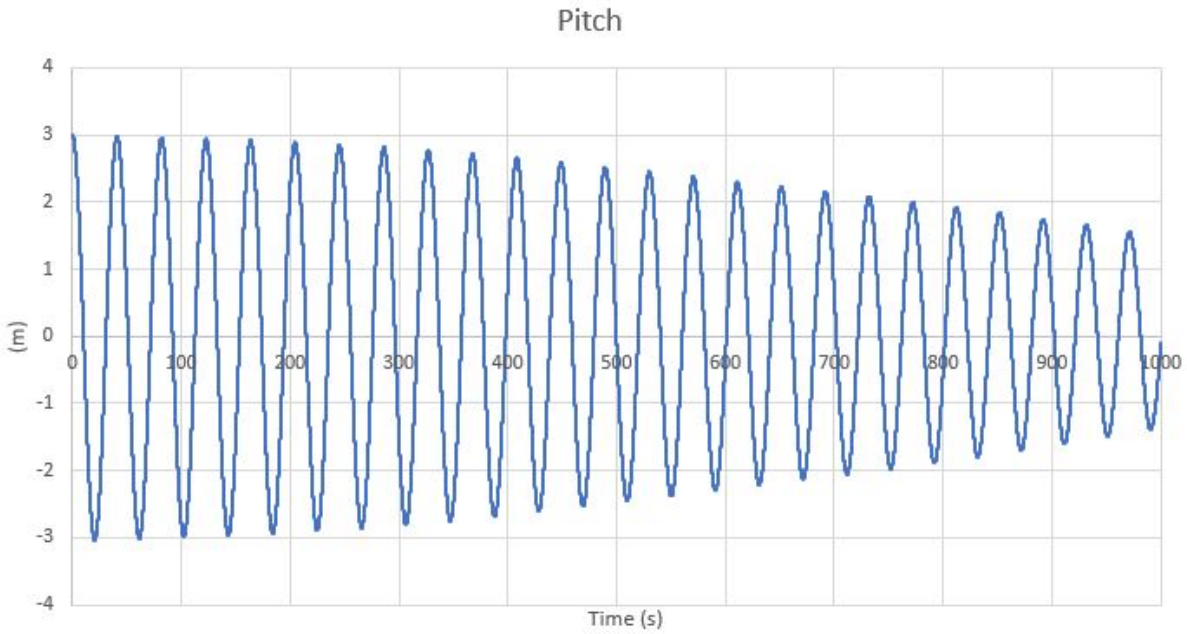

Figure 5.3: Pitch motion for free decay load case.

The natural periods for the motions in study can be found in table 5.10, such as the several intermediate values that are used in the calculations.

Table 5.10: Free decay test results.

Motion	n	t_0	x_0	t_n	x_n	δ	ζ	T_d	T_n
Surge	5	299.250	1.154	854.725	0.0386	0.6795	0.1075	111.10	110.45
Heave	5	503.750	1.774	671.075	1.5950	0.0213	0.0034	33.47	33.46
Pitch	5	367.425	2.719	570.500	2.3760	0.0270	0.0043	40.62	40.61

5.3 Constant wind

Before testing the influence that dynamic loads have on the behaviour of the system, steady state performance is tested. Thus, several simulations with constant wind and no waves were run mainly to test if the mooring system is effective at keeping the platform within an acceptable range. Since the wind is aligned with x-axis, it is the surge motion that will allow this assessment. Figure 5.4 shows the mean offset in surge, but also in pitch. Pitch motion is also important to check the stability of the platform. Too much displacement in pitch can affect the power output of the turbine, because the actual area of the rotor decreases in comparison with a $0°$ situation. In extreme cases, it can lead to the wind turbine shutdown.

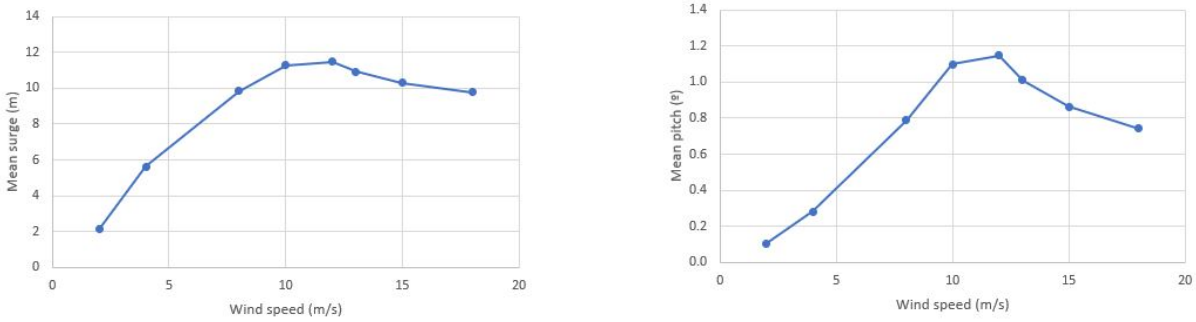

(a) Surge (b) Pitch

Figure 5.4: Mean offset of the platform.

The maximum mean value in both surge and pitch motions occurs at a wind velocity close to the rated wind speed, $12m/s$. Which is coherent with the fact that at rated wind speed there is already a blade pitch angle, that makes the thrust of the rotor become smaller. A maximum mean value of around 12 meters in surge is within an acceptable limit and a maximum of $1.15°$ as well. Actually, according to Roddier et al. [34], the Windfloat platform designed for a 5 to 10MW wind turbine has a limit of $10°$ in operation, making this result around 10 times smaller.

The data gathered with these constant wind load cases can be used to draw the power curve of the upscaled wind turbine, that is presented in figure 5.5.

5.4 Operational load cases

The following simulations show representative load cases of operational conditions under which the wind turbine may have to perform. Table 5.11 has three groups of conditions that were based on the wind velocity, but also in the wave H_s and T_p. Three cases of calm conditions, six moderate and three of

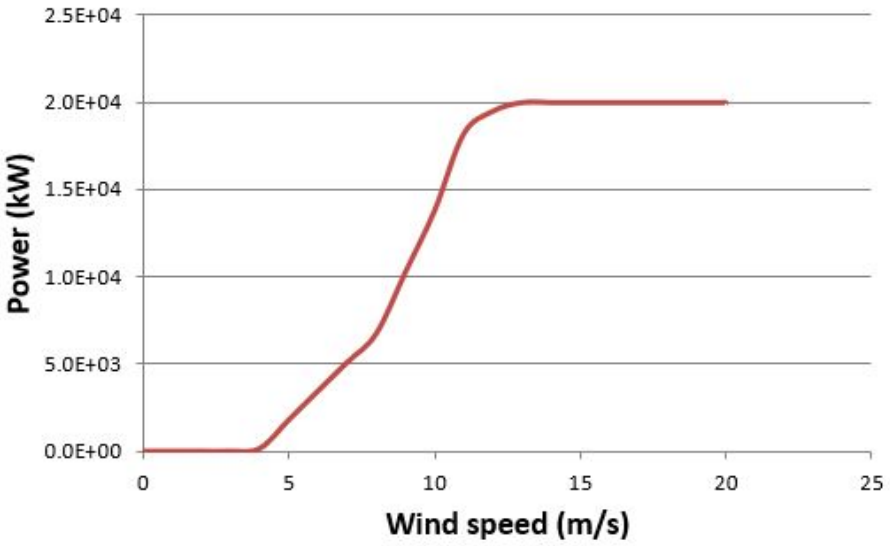

Figure 5.5: Power curve of the 20MW wind turbine.

pre-extreme. In moderate conditions more sea states are represented because these are the most likely to occur when the wind turbine is operating. Although, the system is producing energy in all the load cases represented.

The wind profiles were generated by TurbSim. For all cases, it uses the a IEC Von-Karman turbulence model with class B turbulence intensity. Only the wind speed, which was taken at hub height, changes. Moreover, the stochastic waves are generated by HydroDyn using the JONSWAP spectrum (see 2.2.1). All the simulations have 1000 seconds, but the first 500 seconds are ignored due to transient behaviour, like demonstrated in section 4.2.

Table 5.11: Operational load cases simulated.

Load case	Reference wind speed (m/s)	H_s (m)	T_p (m)
1.1	10	1	8
1.2	10	2	10
1.3	10	3	12
2.1	13	2	10
2.2	13	3	10
2.3	13	4	10
2.4	13	5	10
2.5	13	3	8
2.6	13	3	12
3.1	18	6	12
3.2	18	8	14
3.3	18	10	16

5.5 Dynamic behaviour of the system

The impact of dynamic loads on the system is now tested with the sea states presented in 5.4, neglecting the presence of current. Another external force acting on the turbine is the wind. Table 5.12 shows the mean and standard deviation of the wind speed components used in the three sets of conditions.

Table 5.12: Mean and standard deviation of the wind speed for the simulated conditions.

	Wind speed x (m/s)		Wind speed y (m/s)		Wind speed z (m/s)	
	Mean	Std	Mean	Std	Mean	Std
Calm	9.14	1.95	4.43E-05	1.37	-4.63E-06	1.21
Moderate	11.88	2.19	4.75E-05	1.59	-1.17E-05	1.44
Pre-extreme	16.45	2.62	5.10E-05	1.94	-2.78E-05	1.81

5.5.1 Calm conditions

A summary of the simulation results for the first three cases is represented in the graphs of figure 5.6.

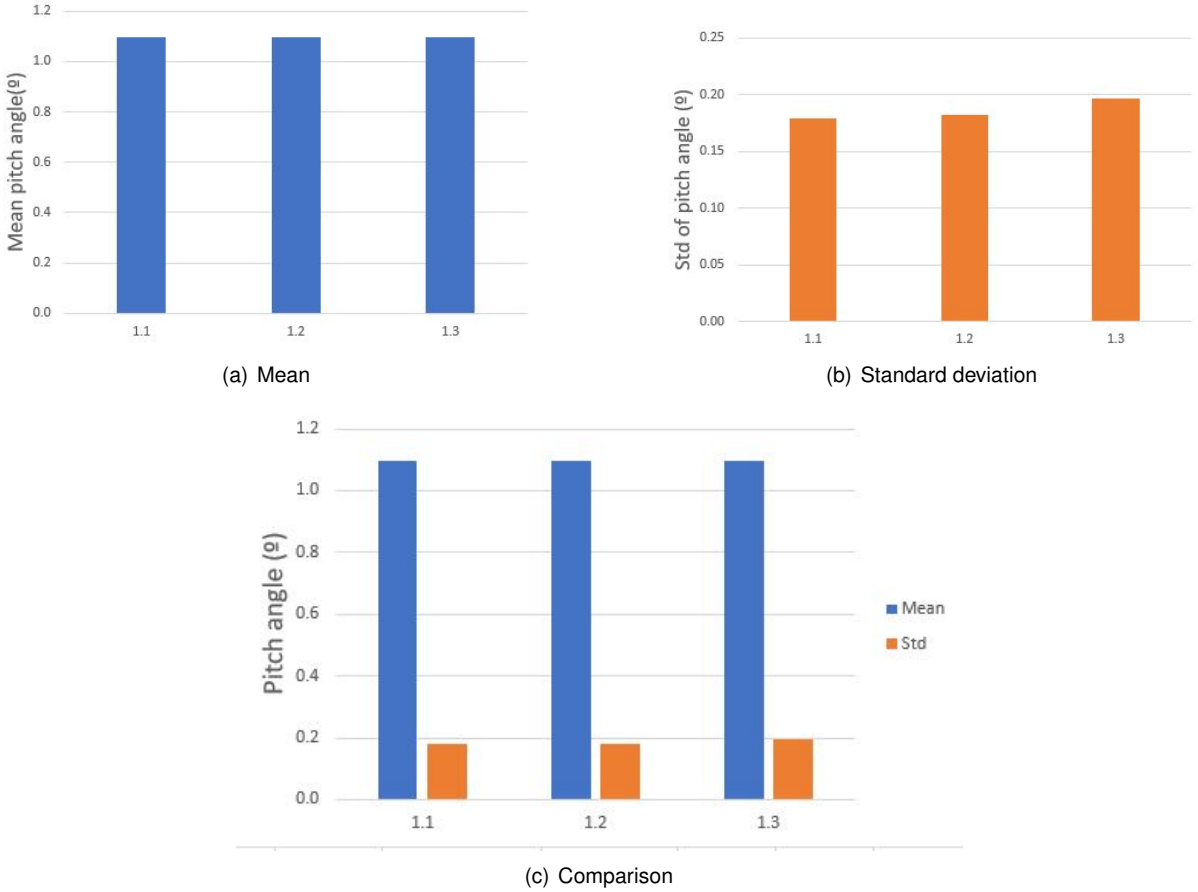

(a) Mean

(b) Standard deviation

(c) Comparison

Figure 5.6: Mean and standard deviation of platform pitch in calm conditions.

There is a slight increase in the standard deviation when H_s and T_p increase. On the other hand, the mean value remains the same. So, one can conclude that these sea states will have little influence in the platform dynamics.

Table 5.13: Mean and standard variation of electrical power output in calm conditions.

Load case	1.1	1.2	1.3
Mean electrical power (kW)	13.9E+03	13.9E+03	13.9E+03
Std of electrical power (kW)	3.50E+03	3.64E+03	3.62E+03

The power output is, as expected, bellow the rated power, since the mean wind speed is bellow rated. The variation caused by the changing sea states is negligible when analysing this output, as one can confirm in table 5.13.

5.5.2 Moderate conditions

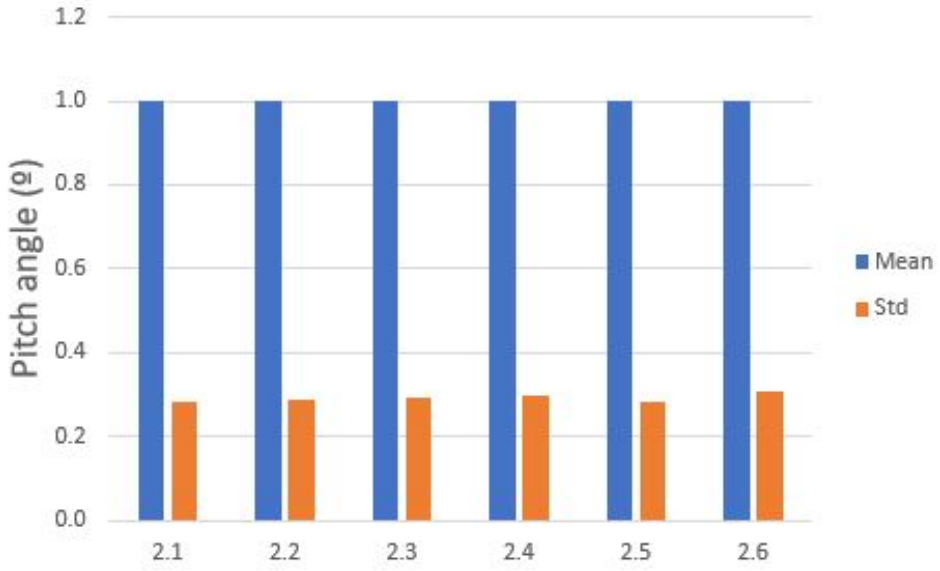

Figure 5.7: Mean and standard deviation of platform pitch in moderate conditions.

Again, the mean pitch of the platform keeps constant independently of the wave significant height and peak period. However, and despite the fact of having small variations, the standard deviation is bigger than in calm conditions. This is the result of a combination of stronger winds and bigger H_s. Looking at the results from figure 5.7, one can observe that T_p has the bigger influence in the standard deviation, because it is load case 2.6 that has the greatest standard deviation. Even though H_s is significantly higher in load case 2.4, the standard deviation is bigger in 2.6 because of the wave peak period.

It is important to note that the mean pitch of the platform is bigger in calm conditions than in moderate. The explanation for this lies on the fact that the controller is not optimized for this turbine. As a consequence, the blade pitch at rated wind speed is already significant, when it should still be zero. This makes the thrust produced by the rotor decrease, reducing the overturn moment and, consequently, making the pitch angle of the platform smaller than it should. In an ideal situation where the controller is perfectly adapted to this turbine, the blade pitch would be null at rated wind speed, but making the controller design from scratch is out of the scope of this work.

The power output is the same for all the load cases, such as the standard deviation. So, one can

Table 5.14: Mean and standard variation of electrical power output in moderate conditions.

Load case	2.1	2.2	2.3	2.4	2.5	2.6
Mean electrical power (kW)	19.5E+03	19.5E+03	19.5E+03	19.5E+03	19.5E+03	19.5E+03
Std of electrical power (kW)	2.60E+03	2.60E+03	2.60E+03	2.60E+03	2.60E+03	2.60E+03

conclude that the magnitude of the sea states is not enough to have an influence on this output.

Even though the reference wind speed is the rated, the power produced is slightly lower than 20MW. There are two main explanations for this. First, the pitch angle of the platform reduces the turbine mean frontal area and the turbulent wind field generated has a mean speed that is bellow rated, as seen in table 5.12. Also, it is important to mention that the platform and, consequently, the turbine are moving in surge and pitch, meaning that the wind acting on the rotor disk is not the real one, but the apparent wind. However, this effect might be very small when compared with the other two mentioned before.

5.5.3 Pre-extreme conditions

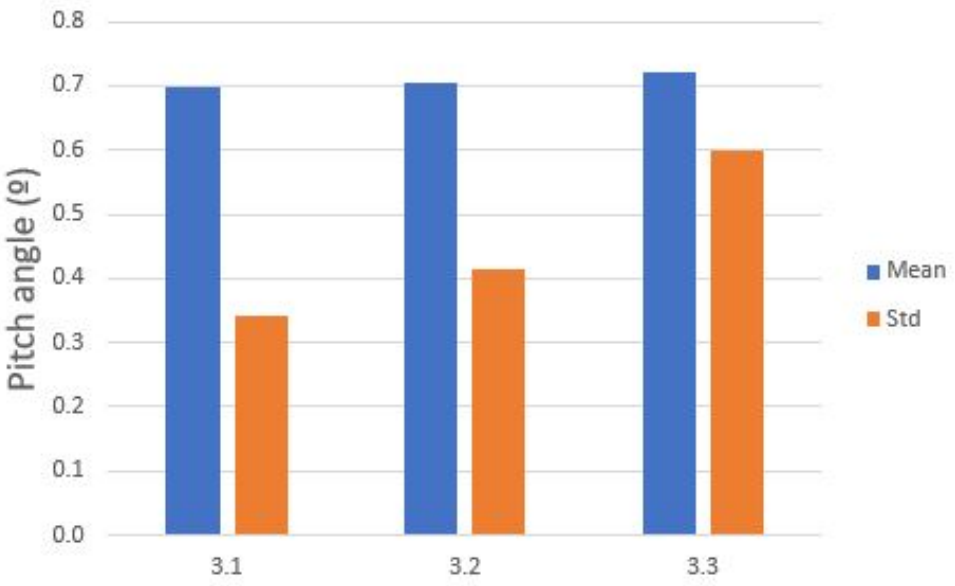

Figure 5.8: Mean and standard deviation of platform pitch in pre-extreme conditions.

Going through load case 3.1 to 3.3, where mean wind speed is above rated and wave conditions are rougher, one can observe in figure 5.8 that mean pitch is lower than in the other cases. This was expected to happen due to the blade pitch increase triggered by greater wind speeds. Although, there is a bigger oscillation than before, as seen by the higher values of standard deviation. For load case 3.3, the standard deviation is close to the mean pitch of the platform, indicating that the pitch angle is spread over a big range of values. Unlike in calm and moderate conditions, where it would always be close to the mean value, because of the low standard deviation, especially in calm conditions.

Load case 3.3 may not represent an operational condition, in a real situation this wave height would likely cause the turbine shutdown. The conditions are close to what a 50-year storm looks like [40]. Nevertheless, the simulation can be carried out by OpenFAST and the power production is ideal, according

to the results presented in table 5.15.

However, it is important to note that the code has limitations, because it considers small displacements of the platform and small wave oscillations. As a consequence, the results obtained for load cases 3.2 and 3.3 might be compromised by this fact, because this range of H_s and T_p is most likely out of the operating upper limit of the code.

Table 5.15: Mean and standard variation of electrical power output in pre-extreme conditions.

Load case	3.1	3.2	3.3
Mean electrical power (kW)	20.0E+03	20.0E+03	20.0E+03
Std of electrical power (kW)	1.59E+03	1.58E+03	1.62E+03

5.5.4 All load cases

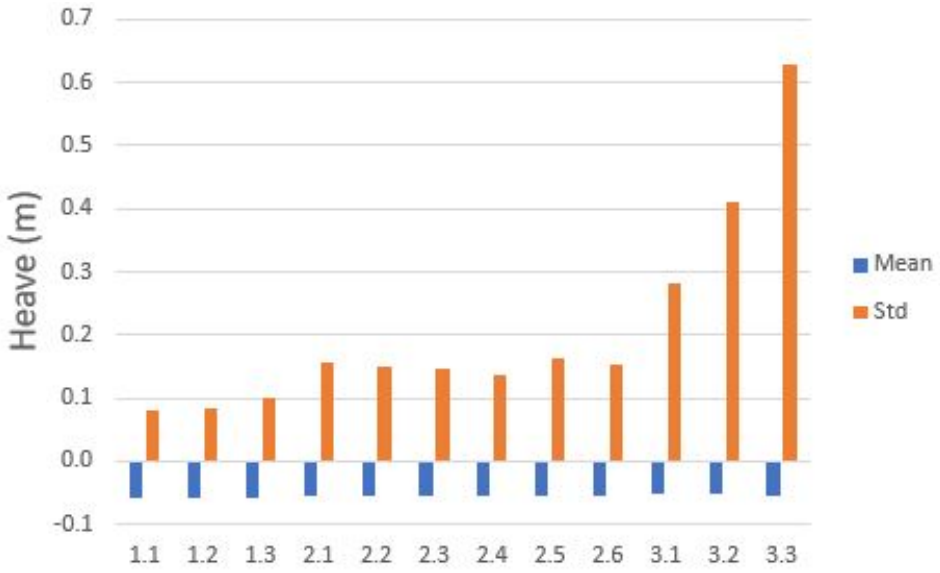

Figure 5.9: Mean and standard deviation of platform heave for all cases.

From figure 5.9, one can observe that throughout several sea states and increasing wind speeds, the mean heave response of the platform always stays constant and very close to zero, its equilibrium position. However, as expected, the standard deviation is significantly higher for the pre-extreme cases, where the significant wave height and peak period are greater. Nevertheless, it is never enough to force the shutdown of the turbine.

Like explained for pitch in 5.5.2, the same happens with the surge motion. The mean value is bigger in calm conditions than in moderate and the cause is the same. This is inevitable due to the high coupling between the two modes. For the pre-extreme cases, the mean displacement is significantly smaller, but the standard deviation increases with the magnitude of the sea states and wind.

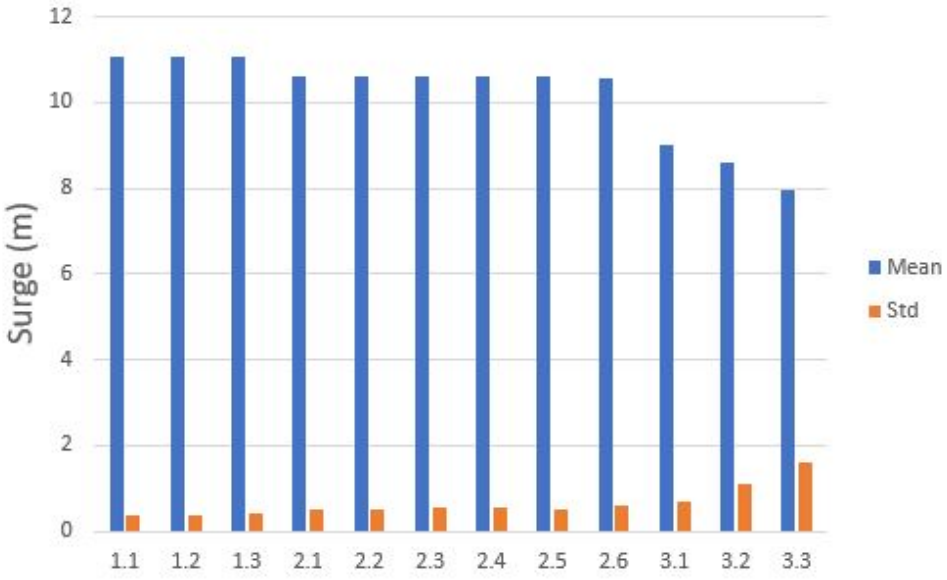

Figure 5.10: Mean and standard deviation of platform surge for all cases.

Chapter 6

Economic model

Floating wind is still in its beginnings and therefore has high costs, especially for prototypes and pre-commercial arrays, like the WindFloat Atlantic project. As the technology is still not totally developed, since there are no commercial scale projects, there is potential to reduce costs of floating wind and reach parity with fixed-bottom wind when deployed at scale.

This chapter presents the tools and methods used in cost prediction. A cost database developed at WavEC is adapted for this case to provide a rough estimation of the LCOE. Finally, ways of reducing the cost of energy are discussed, taking into account the limitations and assumptions of the model.

6.1 Cost competitiveness level of the WindFloat technology

Assessing the costs of a project is essential to check how competitive it can be with other players in the market. Consequently, it is important to analyse where the technology is in terms of its development, because it can give an estimate of how the costs will evolve in the future. One tool for doing so can be seen in table 6.1, the technology readiness level.

Table 6.1: TRL definitions and milestones. [9]

TRL Level	**Milestone**
0. Unproven concept	Idea / preliminary study / patent
1. Proven concept	Desk-based basic design assessment / proof of concept
2. Validated concept	Detailed numerical modelling / structural assessment
3. Prototype tested	Scaled testing (e.g. tank testing, $<$1MW demonstration)
4. Environment tested	Offshore demonstration with 1-5MW turbine
5. System tested	Full-scale demonstration / array with $>$5MW turbine
6. System installed	Full-scale demonstration / array with $>$5MW turbine with $>$1 year operation
7. Field proven	Commercial project

The Windfloat project is currently advancing with its second phase, corresponding to the deployment of three 8MW wind turbines that are schedule to operate 20 to 25 years. Thus, the TRL is level 5 for this case. Analysing figure 6.1, one can see that the costs are at their maximum level. However, they are

expected to go down from here, so the technology should become profitable in the near future.

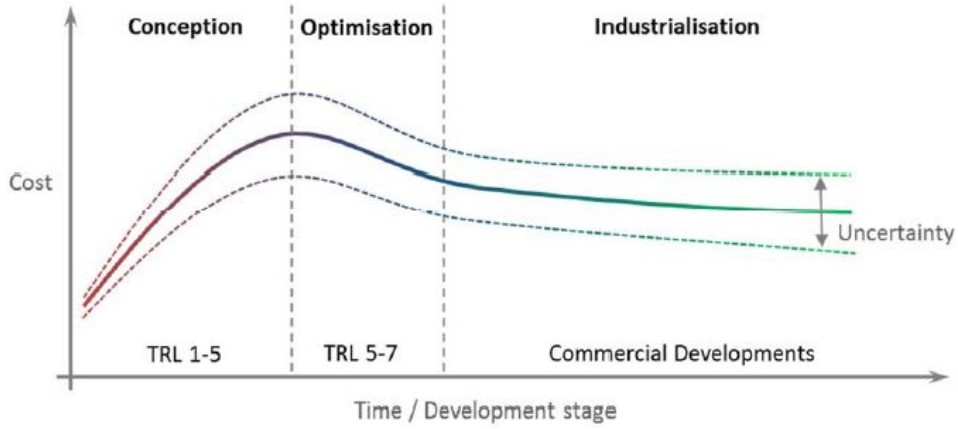

Figure 6.1: Cost evolution of technology through time. [9]

6.2 Levelized cost of energy

The levelized cost of energy measures the lifetime costs of building and operating a power generating device divided by the energy produced in its lifetime. In simple terms, it marks the price at which the energy has to be sold to generate profits.

The project costs can be divided in categories:

- **Capital expenditures (CAPEX):** represents the investment in fixed assets. For this case, a floating wind farm, it is the money invested in acquiring properties and equipment.
- **Operational expenditures (OPEX):** these are the costs necessary to keep the project running. This means operating the farm, which includes rents, maintenance and insurances.
- **Decommissioning costs (DECOM):** costs inherent to reversing the changes made to the location where the project was set up.

When calculating the LCOE, CAPEX and DECOM, that are one time costs, have to be depreciated over the lifetime of the project, N with a discount rate , r. To do this, a capital recovery factor, CRF is used and it differs according to the time of the expense. If it is for a present value, such as CAPEX, equation (6.1) is applied, but for a future expense, like DECOM, one has to use equation (6.2).

$$CRF_{PV} = \frac{r(1+r)^N}{(1+r)^N - 1} \tag{6.1}$$

$$CRF_{FV} = \frac{r}{(1+r)^N - 1} \tag{6.2}$$

Knowing the annual energy production, AEP and that OPEX is an yearly payment, the LCOE can now be calculated as:

$$LCOE = \frac{CRF_{PV} \times CAPEX + OPEX + CRF_{FV} \times DECOM}{AEP} \tag{6.3}$$

This is a summary of the methodology used by the techno-economic model developed at WavEC [41] that is used to execute this part of the research.

6.3 Techno-economic model

6.3.1 Energy production

Wind availability is an important factor when calculating the cost of energy, since a wind turbine can only fulfil its purpose if the wind resource is enough. As this is an initial study, this model assumes that throughout the whole year there is a mean wind speed of 13 m/s at hub height.

The wind speed is considered to vary according to a Weibull distribution from equation (6.4) and it is used to calculate the energy curve from the power curve. The relation between them can be seen in figure 6.2.

The Weibull equation for a probability is

$$f(x, \alpha, \beta) = \frac{\alpha}{\beta^{\alpha}} x^{\alpha-1} e^{-(\frac{x}{\beta})^{\alpha}} \tag{6.4}$$

where α ia the shape parameter, β the scaling parameter and x is the wind speed. In the model is assumed that $\alpha = 2.$ and $\beta = 14.7$. This gives the probability of having a given wind speed, as seen in table 6.2, that is used to determine the energy that the turbine is capable of producing with these conditions.

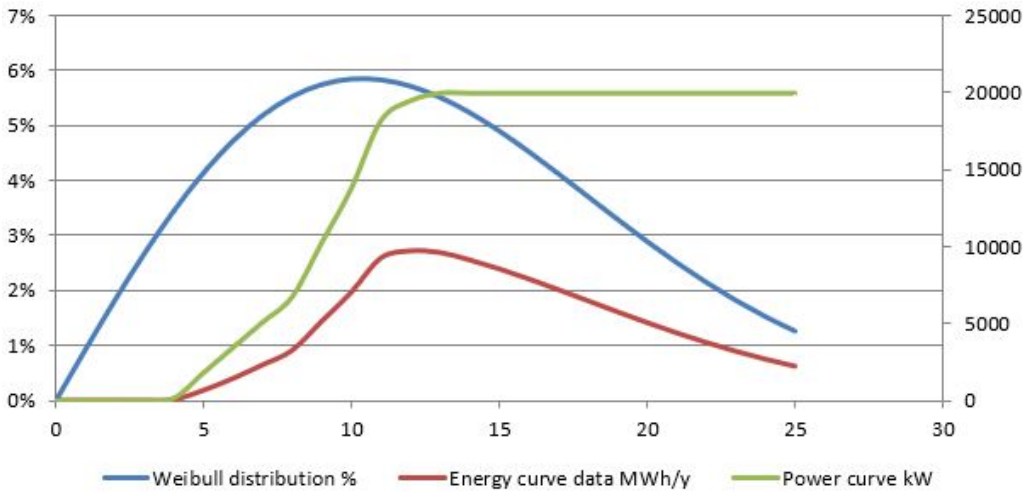

Figure 6.2: Relation between Weibull distribution and power and energy curves.

In an ideal situation with the turbine operating throughout the whole year without stopping at rated wind speed, the total energy it can produce is 175 200 MWh. However, a scenario like that is impossible to achieve. So, with the wind conditions shown in table 6.2, the turbine is able to produce 115 209 MWh per year.

Table 6.2: Wind distribution and energy production.

Wind speed m/s	Weibull distribution %	Energy curve data MWh/y
0	0.0%	0
1	0.9%	0
2	1.8%	0
3	2.7%	0
4	3.5%	48
5	4.1%	655
6	4.7%	1428
7	5.2%	2316
8	5.5%	3266
9	5.7%	5166
10	5.8%	7058
11	5.8%	9290
12	5.7%	9757
13	5.5%	9652
14	5.2%	9169
15	4.9%	8585
16	4.5%	7929
17	4.1%	7226
18	3.7%	6503
19	3.3%	5780
20	2.9%	5075
21	2.5%	4405
22	2.2%	3779
23	1.8%	3205
24	1.5%	2688
25	1.3%	2230
Total	95.1%	115209

Still, the turbine is not always available, it has to be shutdown for scheduled maintenance, for example, and there are losses in electrical transmission. Considering 97% availability and 4.5% of losses, the turbine has an annual energy production, AEP of 106 724 MWh, which corresponds to a 61% capacity factor.

6.3.2 CAPEX

Regarding the breakdown of the CAPEX, it was opted to divide the costs in three categories:

- Project costs;
- Construction and installation;
- Other costs (construction insurance and licensing).

The costs presented in table 6.3 are decomposed based on a floating wind farm cost modelling [42], but most of the data is organized according to the internal database from WavEC.

As the floating platform is regarded, it was opted to assess the cost through the amount of raw materials it is made of, since it is one of the biggest cost drivers for a project like the one in hand. In this case, it is assumed that it is just steel, so the methodology was simply to get the platform weight without ballast from ElastoDyn and multiply it by the price of steel.

- Steel price: $5.18\ \$/kg$ [43]
- Platform weight: $7.8075 \times 10^6\ kg$

Which results in the cost shown in table 6.3. Also, the tower cost is omitted from the table, because it was assumed to be included in the wind turbine cost.

Table 6.3: 20MW wind turbine CAPEX breakdown.

	Cost (k$)	**Cost ($/kW)**	**% CAPEX**
Project costs	4 120	206	4.3%
Development and management costs [44]	1 320	66	1.4%
Engineering costs [44]	2 800	140	2.9%
Construction and installation	91 248	4 562	95.2%
Wind turbine [42]	26 500	1 325	27.6%
Floating Platform	40 443	2 022	42.2%
Installation [9]	15 360	768	16.0%
Mooring system [9]	4 600	230	4.8%
Other construction costs [9, 44]	4 345	217	4.5%
Other project costs	479	24	0.5%
TOTAL	**95 847**	**4 792**	100%

6.3.3 OPEX

Since a 20MW wind turbine is something that has never been done, there are few previews of the magnitude the O&M costs. Thus, it was opted to keep the OPEX breakdown simple and divide it only in the two categories presented in table 6.4. First, the cost of operating the device or wind farm, which includes the rent and insurance, and secondly the costs of maintenance.

Table 6.4: 20MW wind turbine OPEX breakdown.

	Cost (k$)	**Cost ($/kW)**
Operations	620	31
Maintenance	1 240	62
TOTAL	**1 860**	**93**

The OPEX is often represented in terms of the CAPEX, due to the lack of data for cases like this. It was not the approach in this work, but from the values calculated, one cay see that the OPEX is 2% of the CAPEX.

6.3.4 Decommissioning

The techno-economic model used considers that the decommissioning costs are 5% of CAPEX, even though its influence in the LCOE will be negligible.

6.4 Results

With the data necessary already gathered, and knowing that the discount rate is 10% and the lifetime of the project is 25 years, it is possible to estimate a value for the LCOE. Table 6.5 presents the price per unit of energy for CAPEX, OPEX, decommissioning and the LCOE.

Table 6.5: Simplified LCOE.

	$/MWh
CAPEX	98.9
OPEX	17.4
DECOM	0.5
LCOE	116.8

It is important to note that this is just a first assessment and not the most realistic, since this study should be conducted for a wind farm with several turbines and not just one. Although, it provides an initial measure that can be taken as a reference for future work.

Table 6.6 presents the cost breakdown of the several categories and their contribution for the LCOE.

Table 6.6: Total breakdown of the costs.

CAPEX	$/kW	% LCOE
Development and management costs	66	1.2%
Other capital project costs	140	2.5%
Wind turbine	1,325	23.4%
Floating Platform	2,022	35.7%
Installation	768	13.6%
Mooring system	230	4.1%
Other construction costs	217	3.8%
Total	**4 792**	**84.7%**
OPEX	$/kW/y	% LCOE
Operations	31	5.0%
Maintenance	62	9.9%
Total	**93**	**14.9%**
OTHER	$/kW	% LCOE
Decommissioning	240	0.4%
Total	**240**	**0.4%**

The relative proportions of CAPEX and OPEX are 84.7% and 14.9%, respectively. Although, this should be not taken for granted, since the OPEX varies significantly with the distance from shore, but

also with weather conditions and availability of vessels, that may increase the downtime of the turbine.

The greater proportion of all the costs is the floating platform, even though it may be under predicted since only the price of the steel was taken into account. So, as more detailed analysis are done, this proportion is expected to increase even more.

As predicted earlier, the decommissioning costs are negligible, as they represent a percentage of less than 0.5% of the LCOE.

6.4.1 Factors to reduce the LCOE

The LCOE provided by this model with only one wind turbine is not competitive with the current renewable energy solutions. Table 6.7 gives the LCOE estimated in 2018 for onshore wind and solar energy and one can see that they are drastically inferior.

Table 6.7: LCOE for other technologies. [45]

	LCOE ($/MWh)
Onshore wind	55
Solar	70

In order to check whether it is possible to bring down the LCOE, an analysis is conducted by changing some inputs of the model to test their influence on the levelized cost of energy.

Number of devices

The first and more obvious is increasing the number of devices operating in the wind farm. No project on a pre-commercial or commercial stage deploys just one wind turbine.

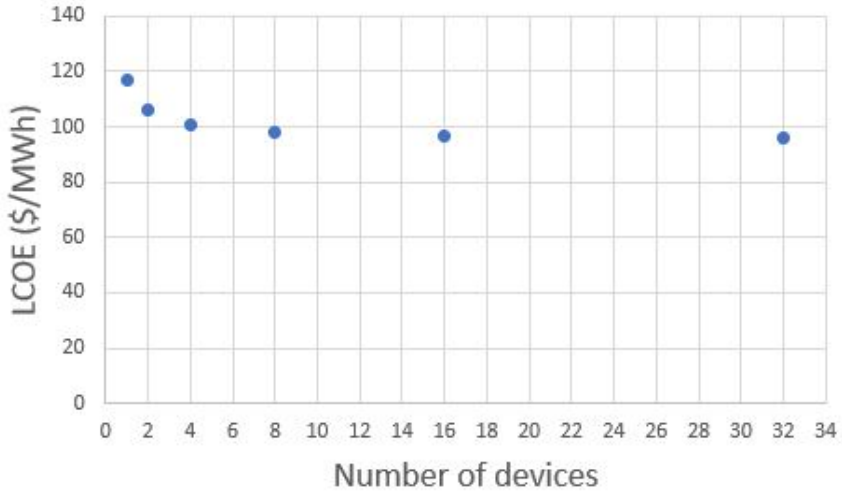

Figure 6.3: Variation of LCOE with the number of devices.

Figure 6.3 shows a decrease on the LCOE from 116.8 $/MWh to around 96 $/MWh, which is better but still not ideal. One would expect it to decrease more sharply, however it does not happen.

The model used to calculate the LCOE considers that when the number of devices increases, the OPEX keeps constant, but the CAPEX increases linearly. So, what is happening is that the LCOE will decrease until the point that the OPEX costs become negligible compared to the rest, which happens when the farm has more than 8 wind turbines.

In fact, a linear increase in CAPEX is not expected. When ordering steel, for example, from a supplier, the price per unit of mass will be lower if the order is 16 turbines instead of just one. This cost reduction is not included in the model, so it can be concluded that in this respect the LCOE is oversized and may go down a considerable amount.

Discount rate

The discount rate of a project plays an important role in the calculation of the LCOE. It will be higher for a project with great uncertainty, such as this one, that is why it was opted to use 10%. Figure 6.4 shows that a less conservative discount rate would decrease the LCOE significantly.

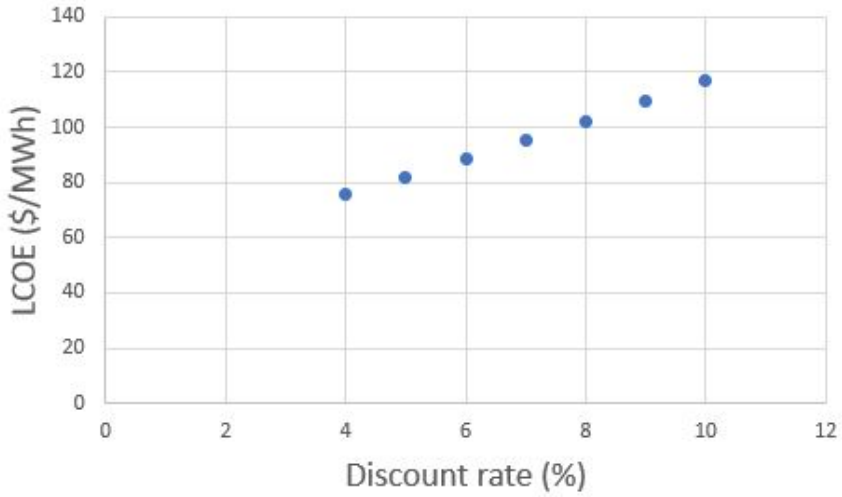

Figure 6.4: Variation of LCOE with the discount rate.

According to [46], for technologies already field proven, both onshore and offshore, the discount rate can go as low as 4.5%. So, one can expect that in the near future, with the advances in technology, the uncertainty of a project of this magnitude will decrease and, as a consequence, it is expected that the LCOE goes down until it becomes competitive in the market.

Weibull shape parameter

The Weibull shape factor is a parameter that reflects the breadth of a distribution of wind speeds. Lower values correspond to broader distributions of wind speed, meaning that winds tend to vary over a large range of speeds. Higher values correspond to narrower wind speed distributions, meaning that wind speeds tend to stay within a narrow range. [47]

Figure 6.5 shows the variation of the LCOE with the shape factor.

There is a significant reduction when the parameter increases. This is explained by the fact that a

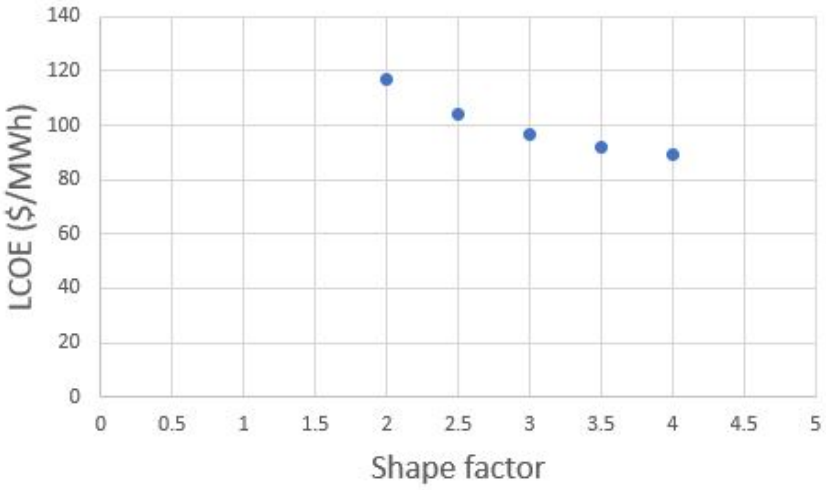

Figure 6.5: Variation of LCOE with the Weibull shape factor.

wind turbine located in a place with a shape parameter of 4 can generate more energy than a turbine where it is 2. This is because a shape parameter of 2 corresponds to a region were the wind is gusty and more irregular than where it has 4. In a region with a shape parameter of 4, the wind is more steady and, therefore, the energy production is bigger, so the LCOE goes down.

Capacity factor

The availability considered for the wind turbine and consequently for the capacity factor is extremely optimistic. The value of 61% is likely to be lower in a real situation, around 40%. As shown in figure 6.6, the LCOE would be higher.

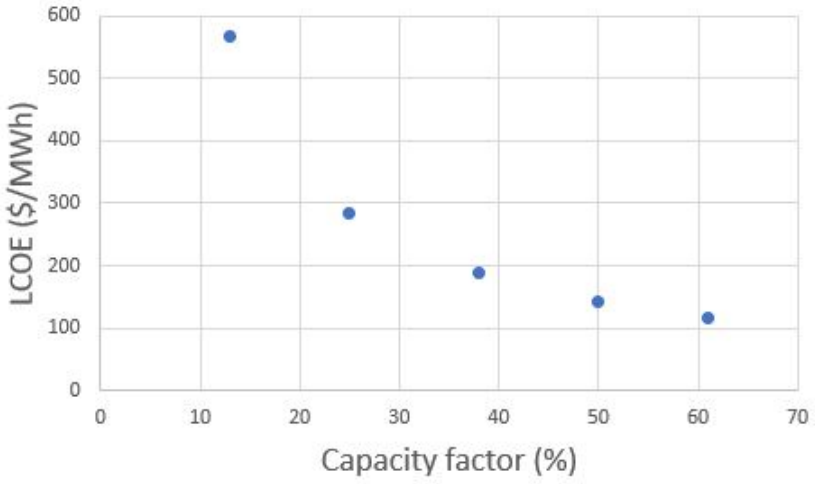

Figure 6.6: Variation of LCOE with the capacity factor.

This is a setback on the path of achieving a competitive LCOE, nonetheless, with the combination of the solutions provided in this sensitivity analysis, the its reduction will be possible.

Chapter 7

Conclusions and future work

This thesis deals with the implementation of a numerical model of a 8MW floating wind turbine in OpenFAST and the scaling procedure towards a 20MW configuration. This study is divided in three phases: estimation of the numerical accuracy of the simulations performed for the 8MW turbine to select the most appropriate numerical settings for the OpenFAST; scale the floating wind turbine to a 20MW configuration and test it under several load cases; make an estimate of the LCOE for the 20MW turbine.

The scaling from 8MW to a 20MW power rating was done because the former has already ongoing projects to deploy turbines of this magnitude, and the latter will mark the future standards in offshore industry. The scaling methodology used in this study can only be used to provide an estimate of the system behaviour under the influence of wind and waves, and the same can be stated about the estimate of the LCOE.

The results obtained in this study suggest that the 20MW floating wind turbine is capable of performing under the conditions tested. Regarding the techno-economic model, it can be concluded that the cost of producing energy with a system of this magnitude can be competitive with other energy solutions in the coming years. The main conclusions from this work are listed as follows:

- An important part of this study was the estimation of the discretization error of the solutions provided by OpenFAST. This allowed to choose the settings for further simulations, such as time step, number of nodes per blade and simulation duration. It can be concluded that the optimal solution in terms of numerical error could not be chosen, because of limited time and computation resources. Nevertheless, the compromise done between accuracy of the solution and the resources gives confidence that in the solutions calculated afterwards with the settings chosen.

- Due to some geometrical uncertainties on the platform dimensions of the WindFloat Atlantic project, the dimensions used for the 8MW model are conservative. After the scaling process was done, the platform oversizing of the 8MW model shifted to 20MW platform. This has to be accounted for when analysing the response of the system to the operational load cases. For the cases 3.2 and 3.3, for wave significant heights and peak periods close to a 50-year storm, with such high mean wind speed, not only the mean pitch, but especially the standard deviation of the response should have higher values. The results obtained show that the turbine could continue

to operate normally, and with significant margin, since the maximum pitch could go up to 10° in a structure of this kind. This allows to conclude that the platform has a good response under the load cases tested, but it could still perform well and be smaller, which leads to savings in terms of manufacturing and logistics and, consequently, to a smaller LCOE.

- The limitations of the economic model allow to conclude that the LCOE that was estimated can be reduced to a point where the technology might become competitive. Deploying bigger wind farms in favourable locations in terms of wind and positioning concerning the O&M logistics, together with development of more reliable technology for a turbine of such great magnitude, seem to indicate that an even lower LCOE than the one of the existing energy solutions can be achieved.

Due to limited scope and time, some topics could not be covered and their discussion in detail is recommended.

- Do the coupled time domain simulations enabling the degrees of freedom corresponding to the vibration of the blades and tower. This requires a pre-processing with another code like NREL's BModes.
- Larger simulations in order to completely remove the transient behaviour effects due to the initial conditions from the results.
- Design a controller from scratch to optimize blade pitching and power production. Also, study the possibility of changing to a direct-drive system.
- Complete the hydrodynamic calculations of the platform with the introduction of the Morrison equation in the model.
- Study more load cases, completing the investigation with wind-wave misalignment and few fault scenarios.
- Complete the techno-economic study with more detailed information on how the O&M costs vary according to numerous factors, like distance to shore, vessel availability or weather windows.

Bibliography

[1] Z. Shahan. History of wind turbines. https://www.renewableenergyworld.com/ugc/articles/2014/11/history-of-wind-turbines.html, November 2014.

[2] W. Europe. wind energy in europe in 2018, trends and statistics, 2018.

[3] R. Siavashi. Sensitivity analysis of the dynamic response of floating wind turbines. Master's thesis, The University of Bergen, 2018.

[4] D. Roddier and J. Weinstein. Floating wind turbines. *Mechanical Engineering Magazine Select Articles*, 132(04):28–32, 2010.

[5] W. Musial, S. Butterfield, and B. Ram. Energy from offshore wind. Technical report, National Renewable Energy Lab.(NREL), Golden, CO (United States), 2006.

[6] W. Europe. Floating offshore wind vision statement. *Wind Europe, Brussels*, 2017.

[7] P. Power. Windfloat presentation, 2011.

[8] F. of Floating Offshore Wind. The future's floating. *Offshore Energy*, 2018.

[9] R. James and M. C. Ros. Floating offshore wind: market and technology review. *The Carbon Trust*, 2015.

[10] P. Technology. Hywind pilot park. https://www.power-technology.com/projects/hywind-pilot-park-aberdeenshire/, 2019. Accessed: 20.09.2019.

[11] Ideol. Floatgen demonstrator. https://www.ideol-offshore.com/en/floatgen-demonstrator, 2018. Accessed: 10.10.2019.

[12] Floatgen. The first operatiional results confirm the excellent performance of ideol's floater. https://floatgen.eu/en/actualites/first-operatiional-results-confirm-excellent-performance-ideols-floater, 2019. Accessed: 10.10.2019.

[13] J. Jonkman. Fast. https://nwtc.nrel.gov/FAST, January 2018. Accessed: 11.08.2019.

[14] J. Jonkman. The new modularization framework for the fast wind turbine cae tool. In *51st AIAA Aerospace Sciences Meeting including the New Horizons Forum and Aerospace Exposition*, page 202, 2013.

[15] B. Jonkman. Turbsim user's guide v2. 00.00. *National Renewable Energy Laboratory-NREL*, 2014.

[16] B. Jonkman and J. Jonkman. Fast v8. 16.00 a-bjj. *National Renewable Energy Laboratory*, 2016.

[17] J. M. Jonkman. Dynamics modeling and loads analysis of an offshore floating wind turbine. Technical report, National Renewable Energy Lab.(NREL), Golden, CO (United States), 2007.

[18] J. M. Jonkman, M. L. Buhl Jr, et al. Fast user's guide. *National Renewable Energy Laboratory, Golden, CO, Technical Report No. NREL/EL-500-38230*, 2005.

[19] T. C. Vinh et al. Determination of added mass and inertia moment of marine ships moving in 6 degrees of freedom. *International Journal of Transportation Engineering and Technology*, 2(1):8, 2016.

[20] J. Jonkman, A. Robertson, and G. Hayman. Hydrodyn user's guide and theory manual. *National Renewable Energy Laboratory*, 2014.

[21] D. Quarton. Wind turbines, part 3: Design requirements for offshore wind turbines. *International Electrotechnical Commission*, 2005.

[22] S. Chakraborty. Ship stability – understanding intact stability of ships. `https://www.marineinsight.com/naval-architecture/intact-stability-of-surface-ships/`, 2019. Accessed: 02.06.2019.

[23] M. OpenCourseWare. Design of ocean systems - lecture 2. `https://ocw.mit.edu/courses/mechanical-engineering/2-019-design-of-ocean-systems-spring-2011/lecture-notes/MIT2_019S11_HydStr1.pdf`, February 2011. Accessed: 02.06.2019.

[24] M. T. Islam. Design, numerical modelling and analysis of a semi-submersible floater supporting the dtu 10mw wind turbine. Master's thesis, NTNU, 2016.

[25] P. J. Moriarty and A. C. Hansen. Aerodyn theory manual. Technical report, National Renewable Energy Lab., Golden, CO (US), 2005.

[26] M. L. Buhl Jr. New empirical relationship between thrust coefficient and induction factor for the turbulent windmill state. Technical report, National Renewable Energy Lab.(NREL), Golden, CO (United States), 2005.

[27] Anonymous. Vestas v164-8.0mw. `https://pdf.archiexpo.com/pdf/vestas/vestas-v164-80-mw/88087-134417.html`, 2019. Accessed: 05.03.2019.

[28] Anonymous. Wind turbine models - vestas v164-8.0. `https://en.wind-turbine-models.com/turbines/318-vestas-v164-8.0#powercurve`, 2019. Accessed: 05.03.2019.

[29] A. Robertson, J. Jonkman, M. Masciola, H. Song, A. Goupee, A. Coulling, and C. Luan. Definition of the semisubmersible floating system for phase ii of oc4. Technical report, National Renewable Energy Lab.(NREL), Golden, CO (United States), 2014.

[30] Anonymous. General description 3mw platform. Technical report, Vestas, 2016.

[31] C. Desmond, J. Murphy, L. Blonk, and W. Haans. Description of an 8 mw reference wind turbine. In *Journal of Physics: Conference Series*, volume 753, page 092013. IOP Publishing, 2016.

[32] J. Jonkman, S. Butterfield, W. Musial, and G. Scott. Definition of a 5-mw reference wind turbine for offshore system development. Technical report, National Renewable Energy Lab.(NREL), Golden, CO (United States), 2009.

[33] C. Bak, F. Zahle, R. Bitsche, T. Kim, A. Yde, L. C. Henriksen, A. Natarajan, and M. H. Hansen. Description of the dtu 10 mw reference wind turbine. *DTU Wind Energy Report-I-0092*, 5, 2013.

[34] D. Roddier, C. Cermelli, A. Aubault, and A. Weinstein. Windfloat: A floating foundation for offshore wind turbines. *Journal of renewable and sustainable energy*, 2(3):033104, 2010.

[35] Demofloat. Windfloat hydrodynamic performance report, 2014.

[36] L. Eça. *Aerodinâmica imcompressível: Exercícios*. IST Press, 2015.

[37] T. Duarte, M. Alves, J. Jonkman, and A. Sarmento. State-space realization of the wave-radiation force within fast. In *ASME 2013 32nd International Conference on Ocean, Offshore and Arctic Engineering*. American Society of Mechanical Engineers Digital Collection, 2013.

[38] A. Jain, A. N. Robertson, J. M. Jonkman, A. J. Goupee, R. W. Kimball, and A. H. Swift. Fast code verification of scaling laws for deepcwind floating wind system tests. Technical report, National Renewable Energy Lab.(NREL), Golden, CO (United States), 2012.

[39] J. George. Windfloat design for different turbine sizes. *UL–University of Lisbon*, 2014.

[40] A. Robertson, J. Jonkman, F. Vorpahl, W. Popko, J. Qvist, L. Froyd, X. Chen, J. Azcona, E. Uzungoglu, C. Guedes Soares, et al. Offshore code comparison collaboration, continuation within iea wind task 30: phase ii results regarding a floating semisubmersible wind system. Technical report, National Renewable Energy Lab.(NREL), Golden, CO (United States), 2014.

[41] W. E. Centre. Techno-economic modelling of wave energy technologies. Updated from v3.7.

[42] G. Katsouris and A. Marina. *Cost Modelling of Floating Wind Farms*. ECN, 2016.

[43] G. B. Elements. Steel prices forecast for 2019. `https://greenbuildingelements.com/steel-building-faqs/steel-prices-forecast/`, 2019. Accessed: 16.09.2019.

[44] T. J. Stehly, P. C. Beiter, D. M. Heimiller, and G. N. Scott. 2017 cost of wind energy review. Technical report, National Renewable Energy Lab.(NREL), Golden, CO (United States), 2018.

[45] V. Henze. Tumbling costs for wind, solar, batteries are squeezing fossil fuels. `https://greenbuildingelements.com/steel-building-faqs/steel-prices-forecast/`, 2018. Accessed: 16.10.2019.

[46] G. Thornton and C. E. Pipeline. Renewable energy discount rate survey results-2018. *Grant Thornton and Clean Energy Pipeline Initiative, Grant Thornton UK LLP*, 2019.

[47] H. Pro. Weibull k value. `https://www.homerenergy.com/products/pro/docs/latest/weibull_k_value.html`, 2019. Accessed: 16.10.2019.